geosciences

Technical Note

Fluid Force Reduction and Flow Structure at a Coastal Building with Different Outer Frame Openings Following Primary Defensive Alternatives: An Experiment-Based Review

Kannangara Dissanayakalage Charitha Rangana Dissanayaka [1] and Norio Tanaka [1,2,*]

[1] Hydraulic Engineering Laboratory, Graduate School of Science and Engineering, Saitama University, 255 Shimo-okubo, Sakura-ku, Saitama-shi 338-8570, Saitama, Japan; kannangara.d.c.r.296@ms.saitama-u.ac.jp
[2] Department of Resilient Society, Research Center for Social Transformation, Saitama University, 255 Shimo-okubo, Sakura-ku, Saitama-shi 338-8570, Saitama, Japan
* Correspondence: tanaka01@mail.saitama-u.ac.jp

Abstract: A well-constructed tsunami evacuation facility can be crucial in a disaster. Understanding a tsunami's force and the flow structure variation across various building configurations are essential to engineering designs. Hence, this study assessed the steady-state flow structure at building models (BM) incorporating outer frame openings, including piloti-type designs with a different width-to-spacing ratio of piloti-type columns following an embankment model (EM) with a vegetation model (VM). The experiments also demonstrated the outer frame opening percentage's impact and orientation toward the overtopping tsunami flow at the BM. The results show that the arrangement of an opening on the outer frame and the piloti-type columns are critical in reducing the tsunami force concerning the experimental setup. Moreover, allowing a free surface flow beneath the BM implies that the correct piloti-pillar arrangement is crucial for resilient structure design. In addition, the three-dimensional numerical simulation was utilized to explain the turbulence intensity of the overtopping flow around the critical BM type. The derived resistance coefficient (C_R) defined the drag and the hydrostatic characteristics at the BM due to the overtopping tsunami flow. Furthermore, for the impervious BM, the value C_R was consistent with the previous studies, while the C_R value for the BMs with an outer frame opening was directly coincident with the percentage of porosity.

Keywords: embankment; building model; vegetation model; outer frame opening; orientation; piloti-type; numerical simulation

check for updates

Citation: Dissanayaka, K.D.C.R.; Tanaka, N. Fluid Force Reduction and Flow Structure at a Coastal Building with Different Outer Frame Openings Following Primary Defensive Alternatives: An Experiment-Based Review. *Geosciences* **2024**, *14*, 287. https://doi.org/10.3390/geosciences14110287

Academic Editor: Denys Dutykh

Received: 16 August 2024
Revised: 16 October 2024
Accepted: 22 October 2024
Published: 26 October 2024

Copyright: © 2024 by the authors. Licensee MDPI, Basel, Switzerland. This article is an open access article distributed under the terms and conditions of the Creative Commons Attribution (CC BY) license (https://creativecommons.org/licenses/by/4.0/).

1. Introduction

The Great East Japan Tsunami (GEJT) in 2011, the Indian Ocean Tsunami (IOT) in 2004, and the Sulawesi Tsunami Indonesia (STI) in 2018 left behind substantial damages and showed that simply identifying coastal zones cannot protect the building structures and coastal infrastructures from potentially catastrophic damage [1,2]. Moreover, broken buildings comprising public, commercial and residential properties, and natural buffers may cause fatal harm to people [3]. Furthermore, numerous researchers have brought various configurations and computational methods into a physical study to evaluate the catastrophic effect of a tsunami on coastal regions, such as ecosystem-based disaster risk reduction (Eco-DRR) or the hybrid defense approach (HDA) [4]. In addition, evacuating people to high ground may not be feasible in some coastal regions, such as peninsulas or coastal areas of extensive flat terrain [5]. Hence, people must be evacuated to the top levels of the tsunami-resistant structures to minimize human casualties. On the other hand, the hydrodynamic component of an impervious building has previously been well-established [6,7]. Furthermore, Dissanayaka and Tanaka [8] have evaluated the flow interaction at single and side-by-side piloti-type pillar arrangements by emergent circular cylinders under different Froude and channel conditions, to identify the associated flow characteristics (surface bow waves, detached hydraulic jumps, wall-jet-like bow wave, and the scouring phenomena).

Following the 2011 GEJT, Chock et al. [9] emphasized the need for a safe building structure design, while Wüthrich et al. [7] highlighted the significance of an opening on the building frame to lower the flood-induced loads under subcritical post-tsunami choked flow conditions. Furthermore, breakaway walls have been recommended by Nakano [10] and Wüthrich et al. [7] to successfully prevent the additional force imposed on the building's structure during flood and tsunami catastrophes. However, such measures did not completely solve the problem. The influence of a building structure's geometry and strength becomes insignificant during the tsunami flow interactions when the tsunami flow forces have been destroyed by the breakaway and internal partition walls [7,11]. The recent post-tsunami survey detailed in the 2018 STI, identified the importance of multi-story buildings such as shopping malls and vertical parking garages, which act as a vertical shelter and can save many lives [7]. Detailed investigation of the loading process due to the tsunami flow interaction, either by direct contact or following primary defensive measures, in terms of forces and submergence characteristics, has become a fundamental tool in determining the fragility curves of a coastal building structure [12–14]. Despite all these advances, scientists could not experimentally manipulate the tsunami-induced loads at a suitable spatial and temporal scale considering the real-world application [1]. Moreover, the GEJT has given researchers a unique chance to comprehensively examine the forces, impacts, and failure processes caused by a tsunami on building structures [9]. Macabuag et al. [15] also discussed categorizing the observed damage patterns and the associated failure mechanisms, which must be considered when designing and evaluating the structural strength, recognizing that a failure may occur due to various forces, effects, and mechanisms.

Most earlier case studies mainly concentrated on the impact forces produced by extremely turbulent, unsteady dam-break-type flows [16], and less attention has been given to the steady-state flow conditions [17]. Moreover, previous studies on the steady-state flow used direct contact with a tsunami overland flow, which did not consider any primary defensive mechanisms such as following a coastal embankment, sea wall, or coastal vegetation [7]. Furthermore, past tsunami events, like GEJT, emphasized that using primary defensive measures could not successfully protect the coastal zone [9,15,18]. This highlights the knowledge gap in terms of estimating the inundation depths and the overtopping tsunami flow-induced forces. As a result, the presented case study aims to pinpoint the tsunami force variation and the flow patterns on the building model (BM) when it is overtopping from a coastal embankment model (EM) without and with a vegetation model (VM). Hence, in this study, the primary objective is the characterization of the tsunami flow force at the BM as it relates to a certain percentage of an opening on the BM frame and the orientation towards the flow, without and with the VM at the EM crest or in the gap region. Moreover, we examined what happens when the BMs were raised using a series of piloti-type circular shape columns, and the flow behavior at the piloti-type arrangement was considered based on the selected overtopping depths from the EM.

2. Experimental Setup and Procedure

2.1. Scaling of the Experimental Model and the Flume Characteristics

To scale the model, water depths measured at the 2004 IOT and the 2011 GEJT were used [4]. The structures frequently occupy a substantial percentage of the available flow channel in heavily populated coastal cities, resulting in partial reflection. Figure 1 depicts an average case for Dickwella town in Matara District, southern coastline of Sri Lanka. During the IOT in 2004, this reach of shoreline experienced extensive damage, including inundation up to a height of 4–10 m, and the recorded damage extent ranged from 600 to 3000 m, respectively. The model scale of the experiment has been described in detail in Figure 1. In Sri Lanka, coastal defensive structures like sea walls and embankments are yet to be constructed. Tanaka et al. [19] proposed a prototype coastal embankment, and the chosen dimensions with a height of 7.25 m and crest width of 3.25 m (see Figure 1 for the location detail). A series of experiments in this study evaluated this prototype design. Then, the model scale was selected to evaluate building destructions due to overtopping tsunami from the proposed coastal embankment. Furthermore, the selected channel satisfied the partial reflection of the flow due to adjacent structures.

Figure 1. The satellite image depicts the selected b_B/W = 0.36 in an actual scale, located in Dickwella, Matara, Sri Lanka: 12.5 m is the actual building width (b_B); 35 m is the approximate channel width (W); p1 and p2 are the sides of the building selected; p3 and p4 are the points on the adjacent structures, which represent the flow channel width.

Therefore, in the present study, the considered length L_s (= L_p/L_m) ratio was set as 50, where L_p is the prototype's length, and L_m is the model's length. The overtopping depths were then assigned to 2.0–6.0 cm, which were consistent with the experimental flume's discharge characteristics. Generally, construction of a coastal embankment is limited to a maximum height of 15.0 m and constructing a more prominent structure would not be possible for a developing country like Sri Lanka. Hence, based on the report of Goff et al. [20] the embankment height should be limited to a maximum height of 7.25 m, and an alternative solution for this study was evaluated downstream. Then, the experimental study was deployed in a glass-sided flume with a zero-bed slope, as shown in Figure 2.

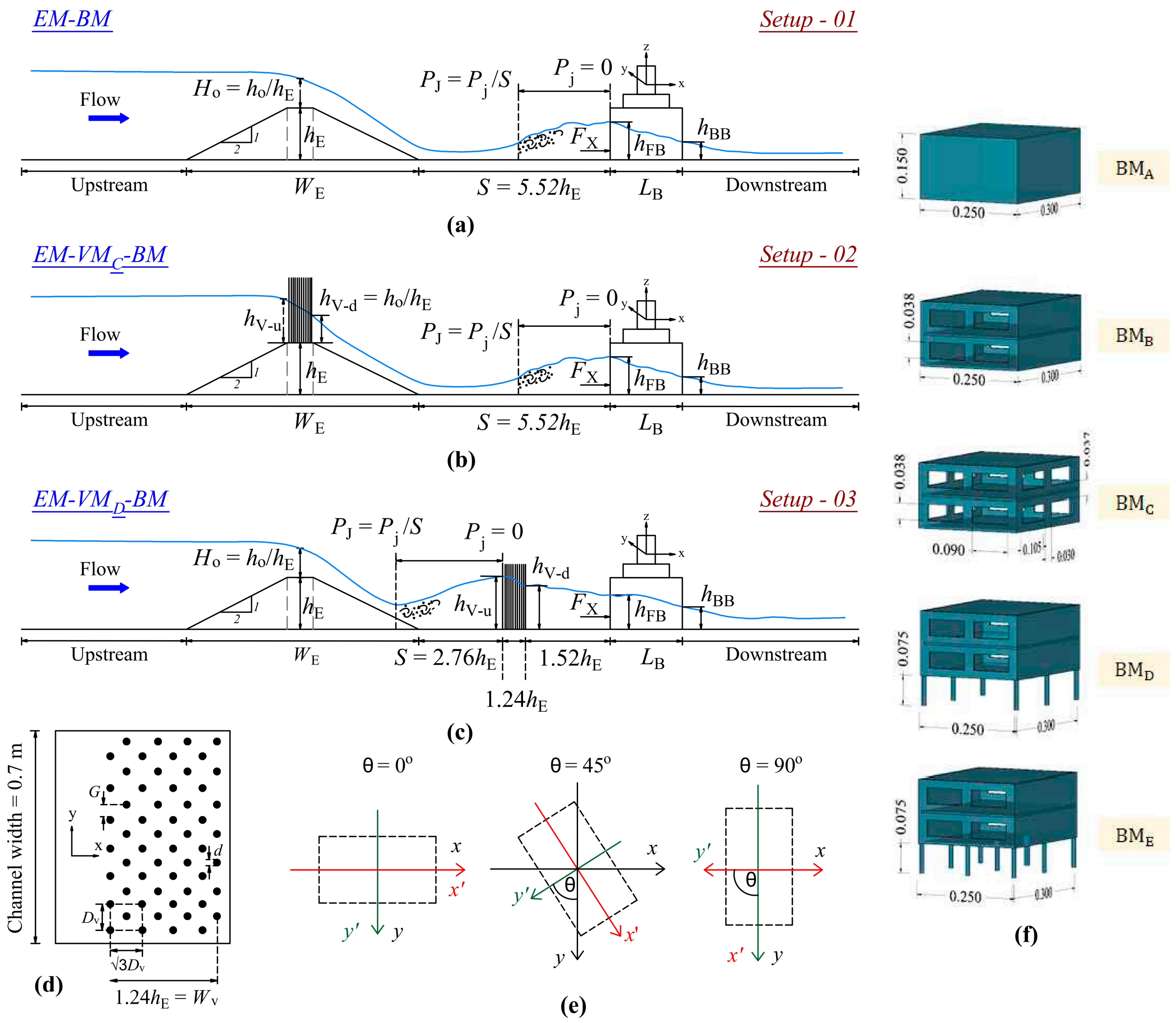

Figure 2. Schematic diagram of the experimental setup, vegetation model, building model rotation, and the types of the building models: (**a**) experimental setup of the EM following a BM as EM-BM, (**b**) experimental setup of the EM following a BM with the VM at the crest of the embankment as EM-VM$_C$-BM, (**c**) experimental setup of the EM following a BM with the VM at downstream of the embankment as EM-VM$_D$-BM, (**d**) details of the VM, (**e**) three rotations considered for the BM, (**f**) details of the building models selected. The notations shown in the figure are as follows: h_E is the EM height, W_E is the length of the EM, L_B is the length of the BM, H_B is the height of the BM, S is the length of the gap region, b_B is the effective width of the BM, h_{FB} is the water depth in front of the BM, and h_{BB} is the water depth in the back of the BM.

2.2. Arrangement of the Experimental Series

Figure 2a depicts the initial case, where the model consists of a completely enclosed BM following an EM at a certain distance from the embankment toe. Based on the selected EM height of 7.25 m for the proposed tsunami-resilient projects in Sri Lanka and Japan, a wooden EM with a height of 14.5 cm and a slope of 1:2 was chosen and assembled on the fixed bed, which was placed on the flume bed, while considering the previous tsunami observation data concerning the land availability [21]. Furthermore, according to Tanaka et al. [19], the selected height of the embankment can withstand a 10.0 m tsunami height, which was proven by the numerical simulation and field observation of 2011 GEJT. In the present experiment, three different experimental conditions have been considered: a

BM following an EM (EM-BM, Figure 2a), a BM following an EM with a VM over the EM crest (EM-$\mathrm{VM_C}$-BM, Figure 2b), and finally a BM following an EM with a VM in the gap region (EM-$\mathrm{VM_D}$-BM, Figure 2c). When selecting the building models, a typical size of a two-story domestic building structure dimensions has been selected [17].

The VM was based on the features of the *Casuarina equisetifolia* and *Pandanus odoratissimus*, which had proven to reduce the tsunami energy on an actual scale with a trunk diameter varying between 0.1 and 0.2 m, respectively [2]. Moreover, to represent the VM, a 0.2 m tree trunk diameter was selected to scale the VM, and the VM was constructed using circular wooden cylinders replicating the main tree trunk [5]. On an actual scale, *C. equisetifolia* and *P. odoratissimus* have a complex emergent root system, representing the vegetation thickness selected in this case study [2]. Furthermore, the selected water depths and water depths observed along the center line of the channel satisfied the defined damage characteristics of *C. equisetifolia* and *P. odoratissimus* as explained by Tanaka [2], where the tree trunk diameter between 0.16 and 0.40 m at breast height (measured 4.5 feet above the ground) can withstand against a tsunami flow depth of 3.5 to 6.0 m, which follows a primary defensive measure like a coastal embankment. In the VM arrangement, the letters d, D_v, and G represent the cylinders' diameter, center-to-center distance, and spacing in the cross-stream direction, respectively, as illustrated in Figure 2d. A cylinder diameter (d) of 4 mm has been selected based on the chosen scale. The constructed VM almost filled the flume width, leaving a small gap between the VM's outermost node and the flume wall. The non-dimensional spacing G/d ratio determined the flow structure around the VM, which was equal to 1.875, used to make the VM over the EM crest as $\mathrm{VM_C}$, and the downstream gap region of the EM as $\mathrm{VM_D}$, as shown in Figure 2. The vegetation model on the EM crest $\mathrm{VM_C}$ was able to protect from the lower overtopping depths, hence, as an alternative solution, the downstream vegetation model $\mathrm{VM_D}$ was selected [22]. The width of the VM (W_v) and the center-to-center distance between the cylinders (D_v) were set based on the vegetation thickness selected $dn\left[=\left(2W_\mathrm{v}/\sqrt{3}D_\mathrm{v}^2\right)10^{-2}\right]$ of 380 No.cm.

Three orientation angles were considered, as shown in Figure 2e, which represent the three b_B/W ratios of 0.36 when $\theta = 0^\circ$, 0.51 when $\theta = 45^\circ$, and 0.43 when $\theta = 90^\circ$ [16,17]. As listed in Table 1, five non-dimensional overtopping depths H_o ($=h_\mathrm{o}/h_\mathrm{E}$) were considered. The BM was kept at a distance equal to 5.52 times of the embankment height (h_E) downstream of the EM (see Figure 2). The reason for having a gap between the BM and the EM was to plant vegetation in the real-scale application and construct other necessary facilities. As shown in Figure 2f, three main BMs were selected based on a two-story building with different frame openings. Three-dimensional models were constructed using lightweight, smoothly coated, 10 mm thick plywood sheets, each with the exact rectangular outer frame dimensions of $0.30 \times 0.25 \times 0.15$ m.

The selected non-piloti-type and piloti-type BMs were categorized based on the total porosity (η_tot), which represents the relative area of the opening as a percentage of the total surface area of the BM's vertical faces. The building model $\mathrm{BM_A}$ has no opening on its frame and represents the total impermeable condition ($\eta_\mathrm{tot} = 0$). The remaining two non-piloti-type building models of $\mathrm{BM_B}$ and $\mathrm{BM_C}$ have different porosities (η_tot) of 16.6% and 35.9%, respectively. The piloti-type connections for the BM selected were considered as the $\mathrm{BM_D}$ with six nos. of piloti pillars and the $\mathrm{BM_E}$ with nine nos. of piloti pillars, respectively (see Figure 2f). The height of the circular cylindrical shape piloti pillar is equal to the single floor height of 7.50 cm according to the selected scale of the present experiment.

Table 1. Experimental setup considered for the present study.

Trial No.	Exp. Case Name	Dimensionless Overtopping Depth (H_o)	Rotation Angle of the BM (deg.), θ	Column Array	Piloti Column Height (cm)
1–15	EM-BM$_A$	0.14, 0.21, 0.28, 0.34, 0.41	0°, 45°, 90°	NP	
16–30	EM-BM$_B$	0.14, 0.21, 0.28, 0.34, 0.41	0°, 45°, 90°		
31–45	EM-BM$_C$	0.14, 0.21, 0.28, 0.34, 0.41	0°, 45°, 90°		
46–60	EM-BM$_D$	0.14, 0.21, 0.28, 0.34, 0.41	0°, 45°, 90°	6 PC	7.5
61–75	EM-BM$_E$	0.14, 0.21, 0.28, 0.34, 0.41	0°, 45°, 90°	9 PC	7.5
76–90	EM-VM$_C$-BM$_A$	0.14, 0.21, 0.28, 0.34, 0.41	0°, 45°, 90°	NP	
91–105	EM-VM$_C$-BM$_B$	0.14, 0.21, 0.28, 0.34, 0.41	0°, 45°, 90°		
106–120	EM-VM$_C$-BM$_C$	0.14, 0.21, 0.28, 0.34, 0.41	0°, 45°, 90°		
121–135	EM-VM$_C$-BM$_D$	0.14, 0.21, 0.28, 0.34, 0.41	0°, 45°, 90°	6 PC	7.5
136–150	EM-VM$_C$-BM$_E$	0.14, 0.21, 0.28, 0.34, 0.41	0°, 45°, 90°	9 PC	7.5
151–165	EM-VM$_D$-BM$_A$	0.14, 0.21, 0.28, 0.34, 0.41	0°, 45°, 90°	NP	
166–175	EM-VM$_D$-BM$_B$	0.14, 0.21, 0.28, 0.34, 0.41	0°, 45°, 90°		
176–190	EM-VM$_D$-BM$_C$	0.14, 0.21, 0.28, 0.34, 0.41	0°, 45°, 90°		
191–205	EM-VM$_D$-BM$_D$	0.14, 0.21, 0.28, 0.34, 0.41	0°, 45°, 90°	6 PC	7.5
206–225	EM-VM$_D$-BM$_E$	0.14, 0.21, 0.28, 0.34, 0.41	0°, 45°, 90°	9 PC	7.5

Note: NP, Non-piloti-type BM; 6 PC, six piloti columns; 9 PC, nine piloti columns.

2.3. Analytical Evaluation of the Force at the Building Model's Front Due to the Overtopping Flow

The horizontal force F_X acting on the impermeable building structure is directly related to the difference in momentum between the upstream and downstream sections [17]. Then, the total drag force F_X can be determined by neglecting the viscous and frictional forces by the following equation:

$$F_X = \rho(M_F - M_B) = \frac{1}{2}\rho g W\left(h_{FB}^2 - h_{BB}^2\right) + \rho W\left(U_{FB}^2 h_{FB} - U_{BB}^2 h_{BB}\right), \quad (1)$$

where ρ (=1000 kg/m^3) is the density of water, g (=9.81 m/s^2) is the gravitational acceleration, W is the width of the channel, h_{FB}, h_{BB}, and U_{FB}, U_{BB} are the water depths and velocities in front (FB) and downstream (BB) of the BM, respectively, as shown in Figure 2. Generally, M is the momentum flux, which is defined as $M = \left(hU^2 + 0.5gh^2\right)W$. This allows us to simplify Equation (1) to Equation (2), which gives a sum of the drag and hydrodynamic components below:

$$F_X = \frac{1}{2}C_D\rho b_B h U^2 + \frac{1}{2}C_H\rho g b_B\left(h_{FB}^2 - h_{BB}^2\right), \quad (2)$$

where C_D and C_H are the drag coefficient and the hydrostatic coefficient, respectively. These are the constants to be determined by an experimental approach and b_B is the transverse width concerning the orientation of the BM. The experiment considered the subcritical approach flow condition upstream of the EM and the Froude number based on the selected overtopping depth (h_o) at the mid-section of the crest of the EM.

The initial Froude number Fr_o refers to the flow depth over the EM crest is given by Equation (3):

$$Fr_o = \frac{U_o}{\sqrt{gh_o}} = \frac{Q_{in}}{h_0 \cdot W\sqrt{gh_0}}, \quad (3)$$

where U_o is the initial velocity measured at the crest of the EM, and Q_{in} is the inlet flow discharge. Moreover, the total drag (see Equation (2)) depends on the porosity of the BM for the non-piloti-type BMs. Equation (4) defines the porosity faced by the upstream water depth as follows:

$$\eta_{tot} = \frac{A_o}{b_B \cdot h_{FB}}, \quad (4)$$

where η_{tot} is the porosity facing the upstream flow depth h_{FB}, which is defined as the ratio between the BM's outer frame opening area A_{o}, and b_{B} is the total building's effective width exposed to the upstream flow. It is worth noting that the rotation angle (θ) of the BM resulted in a larger projected width into the transverse direction, i.e., $b_{\mathrm{B}} = b_{\mathrm{B}=\theta} \cdot (\sin\theta + \cos\theta)$ resulting in larger blockage ratios. Due to the porous properties, Equation (2) must be modified by combining both the hydrostatic and hydrodynamic components with a resistance coefficient (C_{R}) [16,17]. The modified Equation (5) given below, was further tested for the unsteady flow conditions by Wüthrich et al. [7] and steady-state flow conditions by Wüthrich et al. [17], which showed a linear reduction in the total force in the x-direction concerning the openings of the outer frame and the orientation of the BM.

$$F_{\mathrm{X}} = \frac{1}{2}\rho \cdot (C_{\mathrm{R}} \cdot \Phi) b_{\mathrm{B}} h_{\mathrm{FB}} U_{\mathrm{FB}}^{2}, \tag{5}$$

where C_{R} was defined as the resistance coefficient considering both the drag and hydrostatic components for the frontal impervious BM concerning the orientation angle. In Equation (5), Φ is the porosity coefficient, which considers the percentage of an opening of the outer frame on the front, back, and side of the BM via the total porosity of η_{tot}. Moreover, it was defined as the following:

$$\Phi = 1 - \min\left[\eta_{\mathrm{front}};\ \eta_{\mathrm{back}};\ \eta_{\mathrm{side}} \text{ or all}\right], \tag{6}$$

2.4. Measurement of the Forces at the Building Model, Water Depth, and the Velocity

The force exerted on the BM due to the overtopping flow was measured using a tri-axial force gauge with a maximum force measurement capacity of 100 N (manufactured by the SSK Co., Ltd., Tokyo, Japan, and Type LB60-100N, Ser. No. 5640) with an accuracy of 0.1%. The force gauge was fixed over the BM and connected to the flume frame, as shown in Figure 3a. Moreover, a pair of glider mechanisms were fixed to the flume bed that is placed under the BM, as demonstrated in Figure 3b, which avoids direct contact with the base of the BM and reduces friction by keeping a 1.0 mm gap [16]. This configuration allowed the BM to translate the force horizontally (F_x and F_y) after interacting with the overtopping tsunami flow from the EM. Furthermore, the tri-axial force gauge fixed to the BM (see Figure 3a) has been used to quantify the fluid force at the BM while functioning as a solid support to prevent the translation of the BM in three directions of x, y, and z [17]. In addition, for each overtopping depth and case considered, each experiment ran three trials and took the average force value in the respective direction at the BM, which avoids the uncertainties of the hydraulic jump forming in front of the BM after overtopping from the EM [10,16,17]. The average standard deviation of the measured and calculated drag force was 0.354, and the measured drag force with the predicted drag force obtained by Equation (5) was compared to check the variation, as shown in Figure 3c, which depicts the uncertainty was minimal. Moreover, for each experimental run, the tri-axial load cell settings were set to zero for all the directions, which did not account for the BM self-weight. The tri-axial load cell reads voltage fluctuation as a force in the three directions was considered at each experimental run. Then, it was converted to a force according to the calibration chart of the tri-axial load cell provided by the manufacturer [16]. Most of the research articles did not concern the buoyancy and uplift force (F_{Z}), except for the drag force in the x- and y-directions (F_{X} and F_{Y}). In the present study, we evaluated the force in the z-direction (F_{Z}) as a major component that contributed to the stability of the structure during a tsunami flow interaction. Based on the water surface variance throughout the experimental setup (see Figure 2), a point gauge was used to record the water depth at frequent intervals along the center of the experimental flume and where required at interested sections.

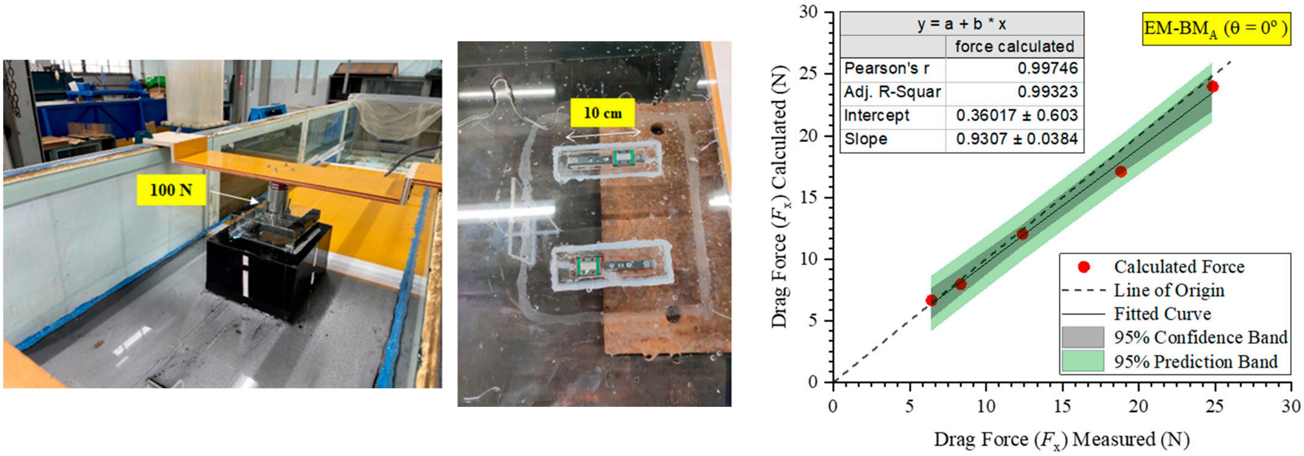

(**a**) (**b**) (**c**)

Figure 3. Experimental settings were used to measure loading on a BM. (**a**) BM$_A$ inside the experiment flume with the load cell arrangement, (**b**) a glider mechanism at the bottom of the BM, (**c**) a correlation plot of drag force measured at the BM$_A$ over the drag force calculated (by Equation (5)) at the BM$_A$ for the EM-BM case.

Moreover, to maintain the accuracy of the data reading, two measuring techniques (image analysis and direct measurement using the gauge reading at the side wall of the flume) were deployed to measure the water surface fluctuations across the selected sections. In addition, water depths at each side of the BM were measured using a gauge reading pasted over the BM's sidewalls concerning the overtopping depth (h_o). An Electromagnetic Flow Current Meter (EFCM) was used to measure the x-directional velocity within the experimental setup at the defined sections, including in front of the BM, back of the BM, sides of the BM, and front and back of the VM, respectively. The EFCM used in this study was the KENEK Corporation Japan (Model No. VM2106 and S/N216552) with an uncertainty of 0.01 m/s.

2.5. Normalized Parameters Used to Define the Mechanism

We suggested a few normalized parameters based on the hydraulic and experimental characteristics of the present study. The normalized overtopping depth was defined as $H_o = h_o/h_E$, where h_o is the overtopping depth measured at the mid-section of the EM crest, and the h_E is the EM height. Five H_o values were selected and listed in Table 1. The normalized position of the detached hydraulic jump was defined as the $P_J = P_j/S$, where P_j is the position of the hydraulic jump toe within the experimental domain, as shown in Figure 2a,c, and S is the free space between the EM toe and the starting position of the BM front face for the EM-BM and EM-VM$_C$-BM cases, respectively. For EM-VM$_D$-BM, S is the free space between the EM toe and the upstream of the VM (Figure 2c). Formation conditions of the hydraulic jump were based on the BM's porosity (Figure 2f) and the rotation angle (Figure 2e). As a result, the distance between the subsequent section considered and the starting point of the hydraulic jump was used to determine the position of the jump (P_j). The overtopping depth was normalized by the upstream-to-downstream water depth reduction in the non-piloti-type BM $H_C^* \; [= (h_{FB} - h_{BB})/h_o]$, which explains the relationship of the force reduction at the BM due to the choked condition [17]. Moreover, a normalized resistance coefficient was defined as the $C_R^* \; (= C_R/C_{R,0})$ where C_R is the resistance coefficient, which represents the drag characteristics, and $C_{R,0}$ is the resistance coefficient of the entirely impervious BM as denoted in Equation (5).

2.6. Numerical Model Setup, Boundary Condition, and Calibration

For the numerical simulation, the open source algorithm called OpenFOAM-v2106 has been used based on Reynolds's Average Navier Stokes Equation (RANS) and with the two-phase numerical solver called Volume of Fluid Method (VOF) for the present study, as described by Dissanayaka et al. [23]. The numerical model considered three mesh grids, which have a total number of cells of about 1,213,268 (Mesh 1), 468,768 (Mesh 2), and 579,265 (Mesh 3), respectively. Three turbulent models called the k–ε, RNG k–ε, and k–ω SST were used for the numerical model to identify the most suitable turbulence model and continue the numerical simulation. Mesh refinement was used to refine the mesh within the sections of 0.7 m to 2.5 m, and the BM was located between 1.94 m and 2.24 m, as shown in Figure S1 in Supplementary Figures. The refinement region captures the flow structure variation over the upstream and downstream of the building model concerning the porosity properties considered.

To achieve the steady-state flow condition, a "variableHeightIntletFlowRateVelocity" boundary condition (BC) was used for the inlet, which defines the two-phase flow condition. The bottom of the flume, embankment, and building models were employed to derive the "no-slip" BC. For the no-slip BC, the velocity was zero, and the pressure was assigned as "fixedFluxPressure" BC, while the standard wall function ("omegaWallFuntion" BC) was used for wall shear stress. A "zeroGradient" BC (Neumann BC) was defined as the outlet of the numerical domain. In addition, the "inletOutletPressure" BC was employed (see Figure S1 of Supplementary Figures). According to the OpenFOAM user manual, the BC notations mentioned above are the standard [24–26]. In addition, an explanation of the general equation, free-surface modeling, turbulence models used, model stability, time step control, and statistical indicators used to evaluate the numerical model results are explained in the "Supplementary Notes". Moreover, for the numerical model, the initial water depth was set up to the crest level of the EM to minimize the numerical diffusion. The numerical simulations were ran for a conservative duration maximum of 60 s, which secured the steady-state condition, and the ParaView software was used to carry out the post-processing [23].

3. Results

3.1. Flow Structure Within the Experimental Domain for the EM Following a BM Without the VM

Figure 4 shows the flow structures through the experimental domain with different types of BM without any rotation ($\theta = 0^\circ$) following an EM for the experimental case EM-BM. In this study, four basic flow types were observed, i.e., Type-1 (see 2–5 cm results in Figure 4a) and Type-2 (see 6 cm results in Figure 4a) hydraulic jump within the gap region of the BM and the EM. Furthermore, a bow wave including a detached hydraulic jump (see Figure 4b) and the wall-jet-like bow wave (see Figure 4c) at the front face of the BM as well as the front face of the piloti-type column have been observed, respectively [6,8]. Moreover, the hydraulic jump was classified based on the location of the jump toe. When the hydraulic jump toe was lying within the gap between the EM and BM, the jump was identified as a Type-1 hydraulic jump, and when the starting position of the hydraulic jump was observed on the downstream surface slope of the EM, the jump was defined as a Type-2 hydraulic jump [27].

Moreover, when the BM had a specific porosity (like $\mathrm{BM_B}$ and $\mathrm{BM_C}$), the overtopping flow becomes supercritical in the gap region, while forming a detached hydraulic jump with a bow wave due to the flow passing through the BM, as shown in Figure 4b. Meanwhile, when increasing the overtopping depth from the EM, the detached length slightly increased, while the bow wave running along the front face of the BM was extended for the $\mathrm{BM_B}$ and $\mathrm{BM_C}$ (see Figure 4b). When the BM was elevated by using an array of piloti-type columns, no hydraulic jump formed due to the arrangement of the piloti-type columns, which allowed a free flow below the BM (see Figure 4c). This phenomenon was classified as a no-jump except for the wall-jet-like bow wave in front of the piloti-columns. Furthermore, a similar flow phenomenon has been observed when increasing the water depth within the cylinder array below the BM, as shown in Figure 4c [8,16].

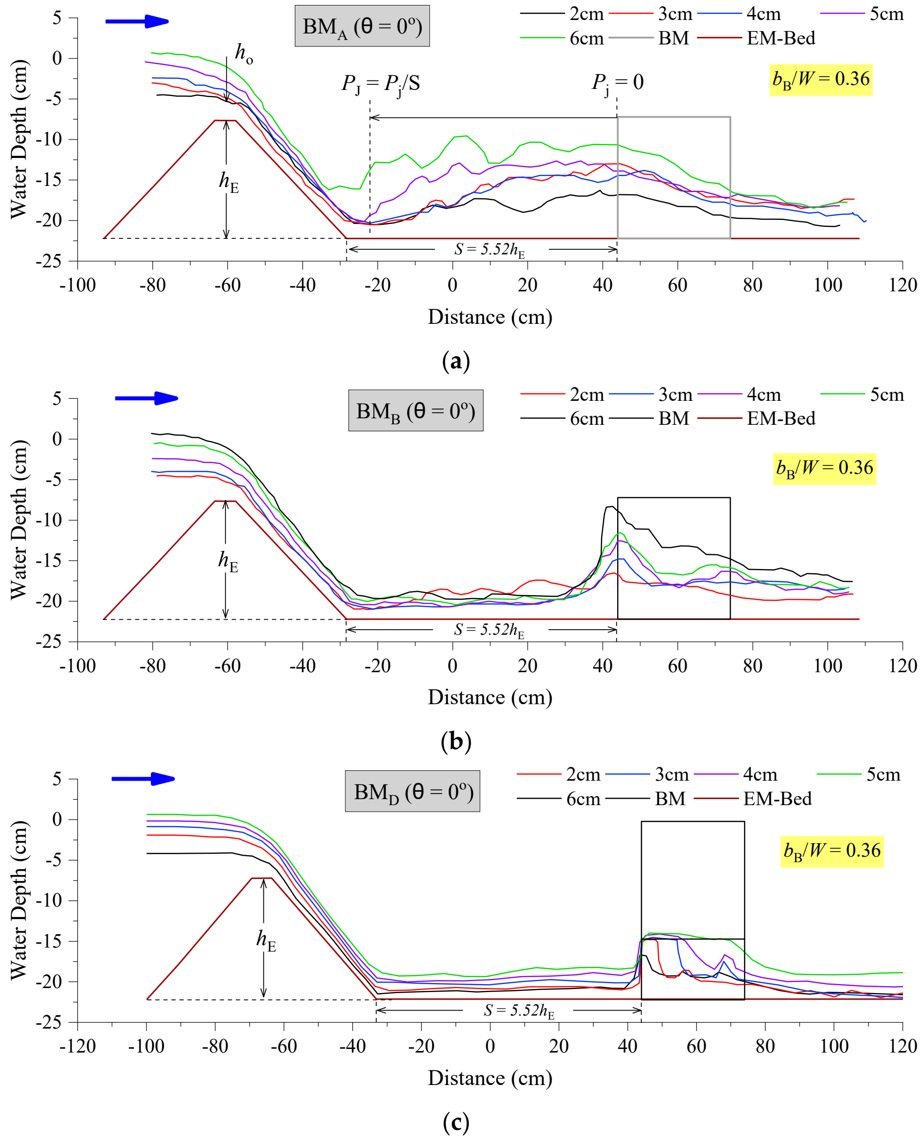

(**a**)

(**b**)

(**c**)

Figure 4. Flow structures across the EM-BM case for the zero-degree rotation angle (θ = 0°, b_B/W = 0.36): (**a**) BM$_A$, (**b**) BM$_B$, and (**c**) BM$_D$ (the blue arrow shows the direction of the flow). Additionally, Figure 4a shows the height of the EM (h_E), overtopping depth (h_o), the position of the hydraulic jump (P_j), and the distance between the EM toe and the BM (S).

Moreover, to characterize the flow behavior at the non-piloti-type BMs, the ratio of the non-dimensional water depth H_F $(= h_{FB}/h_E)$ measured in front of the non-piloti-type BM, obtained for the highest non-overtopping depth H_o $(= h_o/h_E)$, presented in Figure 5 as a function of the Froude number (Fr_{FB}), was measured in front of the BM for the EM-BM case. The results presented in Figure 5 show that a Type-2 hydraulic jump was generated when the BM frontal water depth exceeded the limit of 0.5 times the embankment height (h_E). The hydraulic jump-starting point was lying on the EM downstream surface slope with a subcritical Froude condition concerning the BM total porosity (η_{tot}) and the orientation angle (θ). Furthermore, with the increased porosity of the BM towards the flow direction, the Type-2 hydraulic jump was converted to a Type-1 hydraulic jump or detached bow wave, as shown in Figure 4b [16,17]. The error bars in Figure 5 represent the standard deviation of the measured water depths in front of the BM for all the approaching flow depths under the EM-BM case. In addition, the hydraulic jump formation conditions concerning the experimental setup are discussed in the next section.

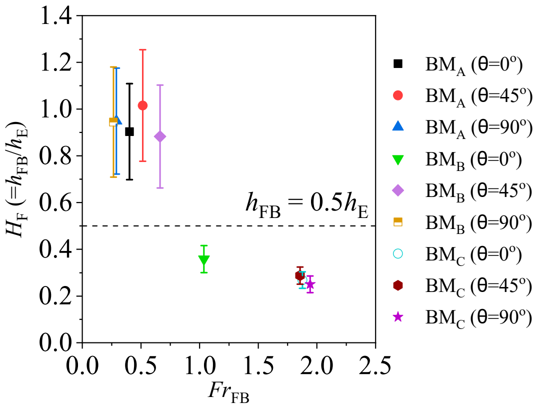

Figure 5. Water depth in front of the building model H_F (=h_{FB}/h_E) relative to the embankment height for non-piloti-type buildings over the Froude number (Fr_{FB}) measured in front of the BM for the EM-BM case under the maximum non-dimensional overtopping depth of h_o/h_E = 0.41.

3.2. Numerical Model Sensitivity and Validation

The numerical model's sensitivity to the grid size and the chosen turbulence model were assessed utilizing a statistical indicator such as the root mean square error (RMSE), normalized root means square error (NRMSE), normalized mean square error (NMSE), mean absolute percentage error (MAPE), mean absolute error (MAE), and determination coefficient (R^2) [23,28,29]. To check the model sensitivity, over the mesh resolution, the numerical model simulated for the non-overtopping depth H_o equals to 0.41 (see Table 1) was evaluated. The numerical model sensitivity analysis was conducted with the control case, which used BM_A when the rotation angle (θ) equals zero.

The results of the numerical model sensitivity based on the streamwise velocity (U_x) are listed in Table 2 and concern the grid size and the turbulence model selected using the listed indicators. From the sensitivity results listed in Table 2, the highest correlation was given by the k–ω SST turbulence model for Mesh 1. Furthermore, Figure S2 in the Supplementary Figures shows the streamwise horizontal velocity profiles observed over the embankment crest concerning the mesh and the turbulence model selected in the numerical model calibration. According to the results shown in Figure S2, the velocity profiles belong to Mesh 1, showing good agreement between the numerically predicted velocities and the experimentally observed velocity profile for the k–ω SST turbulence model.

Moreover, to check the accuracy of the developed numerical model, the accuracy of the predicted and measured water surface profile along the channel center line, concerning the mesh and the turbulence model selected, was evaluated. The free surface obtained by the numerical simulation, performed with the VOF, and each turbulence model selected concerning the mesh is shown in Figure S3 of Supplementary Figures. According to Figure S3a, the calculated free surface profile for the k–ω SST turbulence model reasonably matched the measured profile of the other two. However,, when reducing the number of cells in the numerical grid, as shown in Figure S3b,c, the accuracy of the free surface of the numerical prediction was reduced, which concerned the measured profile in the experimental study. According to Figure S3a, k–ω SST turbulence model captured the formation conditions of the hydraulic jump toe and the entire free surface profile than the other two selected. Therefore, according to the data in Table 2 with the graphical representations in Figures S2 and S3, the k–ω SST turbulence model was selected to carry out the numerical simulation in this study.

Table 2. Sensitivity analysis of the computed streamwise velocity at the mid-section of the embankment over the selected grid size and turbulence model.

Turbulence Model	Mesh & No. of Cells	RMSE	NRMSE	NMSE	MAPE	MAE	R^2
k–ω SST	Mesh 1 (1,213,268)	0.007	0.091	0.009	0.006	0.004	0.919
k–ε		0.007	0.090	0.009	0.005	0.006	0.906
RNG k–ε		0.015	0.194	0.037	0.014	0.012	0.895
k–ω SST	Mesh 2 (468,768)	0.010	0.127	0.020	0.008	0.007	0.860
k–ε		0.015	0.213	0.056	0.012	0.011	0.757
RNG k–ε		0.013	0.135	0.022	0.012	0.010	0.886
k–ω SST	Mesh 3 (579,265)	0.011	0.141	0.026	0.010	0.009	0.845
k–ε		0.012	0.146	0.020	0.011	0.008	0.881
RNG k–ε		0.014	0.157	0.029	0.014	0.012	0.887

3.3. Hydraulic Jump Formation Concerning the Experimental Setup

After the flow interacts in front of the BM, a submerged hydraulic jump occurs when the flow changes from a supercritical to subcritical condition after overtopping from the EM. For the present study, the type of hydraulic jump forming in a rectangular prismatic channel with a zero upstream slope and nearly horizontal downstream slope are characterized using the non-dimensional overtopping depth (H_o). The quick dissipation of the overtopping flow from the EM increased the safety of the BM when it had enough opening space in its frame while flowing through it. This experimental study observed a hydraulic jump between the downstream gap region between the EM toe and the BM front or EM toe and the VM front (see Figure 2a–c) concerning the experimental arrangement. Out of the selected BMs, the $\mathrm{BM_A}$ and $\mathrm{BM_B}$ gave more attention due to their geometric arrangement, as shown in Figure 2f. Figure 6 shows the normalized position of the hydraulic jump over the $\mathrm{BM_A}$ and $\mathrm{BM_B}$ according to the experimental settings of EM-BM and EM-$\mathrm{VM_C}$-BM, respectively.

To define the location of the hydraulic jump in this study, three values of the non-dimensional position of the hydraulic jump P_J (= P_j/S) were defined based on the starting position of the jump within the system, which was measured according to the BM front or VM front, as shown in Figure 2a–c. When the non-dimensional position of the jump was $P_J < 1$ the hydraulic jump's starting position was within the gap region when $P_J = 1$ the hydraulic jump's starting position was on the EM's toe, and when $P_J > 1$ the hydraulic jump's starting position was on the EM's downstream surface slope as shown in Figure 4a [22]. For the piloti-type BMs ($\mathrm{BM_D}$ and $\mathrm{BM_E}$), the P_J value was not calculated due to the absence of a hydraulic jump except for the bow wave along the piloti-column surface. Moreover, in front of the $\mathrm{BM_C}$, the wall-jet-like bow wave was observed with a detached hydraulic jump while increasing the overtopping flow from the EM, which is because the porosity of the $\mathrm{BM_C}$ promoted quick dissipation of flow from its four-sided opening, as shown in Figure 4b. When a Type-1 hydraulic jump formed, the value of the P_J was less than 1, as shown in Figure 6, with a $\mathrm{BM_A}$ and $\mathrm{BM_B}$ under the experimental cases of EM-BM and EM-$\mathrm{VM_C}$-BM, respectively. Additionally, when the overtopping flow depth increased, the hydraulic jump position moved closer to the embankment toe, and when the P_J was greater than 1, the hydraulic jump position was seen on the downstream surface slope of the EM while rotating both the BMs, as shown in Figure 6. Furthermore, when a hydraulic jump transferred to Type-2 from Type-1, the water depth in front of the BM increased. This phenomenon further increased the force at the BM. The increasing water depth in front of the BM was directly related to its total porosity (η_{tot}) and the orientation angle (θ).

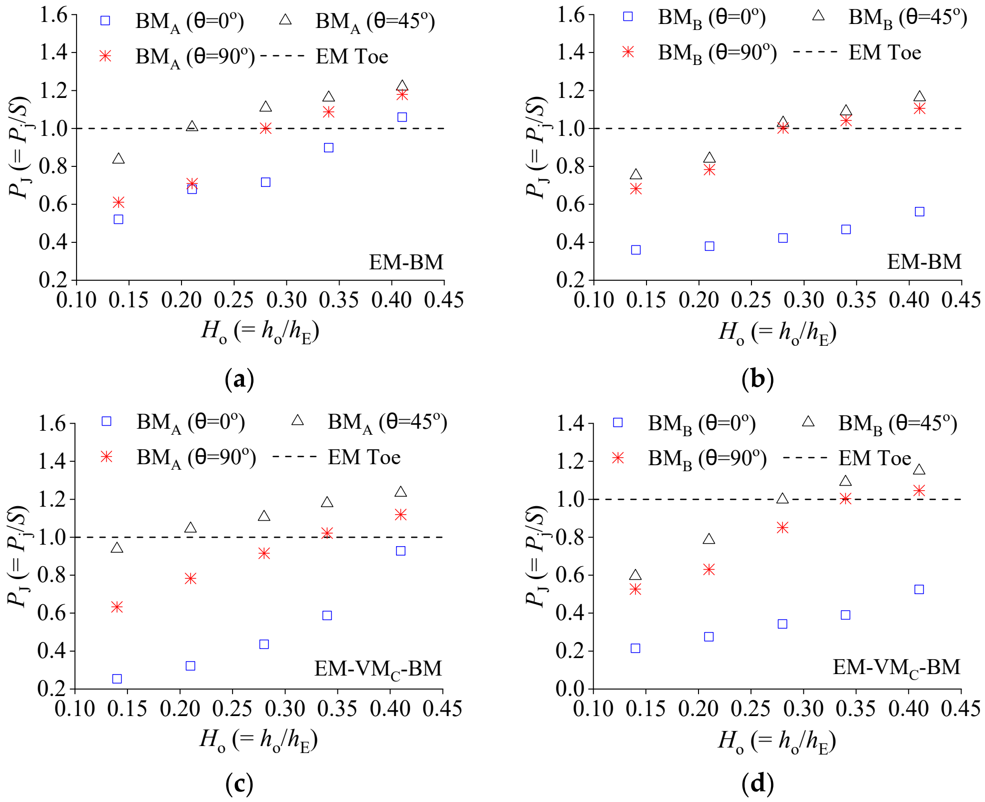

(**a**) (**b**) (**c**) (**d**)

Figure 6. Normalized position of the hydraulic jump P_J (=P_j/S) over the normalized overtopping depth H_o(=h_o/h_E) according to the orientation angle and the experimental setup considered: (**a**) BM_A with the EM-BM case, (**b**) BM_A with the EM-VM$_C$-BM case, (**c**) BM_B with the EM-BM case, and (**d**) BM_B with the EM-VM$_C$-BM case.

According to the experimental EM-VM$_D$-BM case, the hydraulic jump was observed within the gap region of the EM toe and VM front, as shown in Figure 2c. Moreover, for all the BMs used under the experimental EM-VM$_D$-BM case, while increasing the overtopping depth, Type-1 and Type-2 hydraulic jump was observed. Figure 7 shows the relative position of the hydraulic jump over the non-dimensional overtopping depth (H_o) for the EM-VM$_D$-BM case. In this case, the hydraulic jump position was measured from the VM front towards the EM toe, as shown in Figure 2c. The VM in the gap region (see Figure 2) absorbs the turbulence of the overtopping flow and slows down the flow velocity toward the BM. The velocity towards the VM downstream completely depends on the VM thickness (*dn*); while lowering the vegetation thickness, the flow velocity of the VM downstream also increases and vice versa. As shown in Figure 7a,b, the Type-2 hydraulic jump was further extended with the BM_A and BM_B under the experimental EM-VM$_D$-BM case. For the BM_C, due to the VM in the gap region, the wall-jet-like bow wave converted to a hydraulic jump under the EM-VM$_D$-BM case while increasing the flow depth in front of the BM_C.

Meanwhile, for the EM-VM$_D$-BM case, the formation conditions of the wall-jet-like bow wave had vanished except for the submergence of the piloti-type columns of the BM_D and BM_E while increasing the overtopping depth from the EM. In addition, Figure 7d,e shows that piloti-type BM would be the most appropriate hybrid approach to reduce the formation of the Type-2 hydraulic jump which could facilitate the reduction in the self-destruction of the embankment structure under disastrous situations on the prototype scale [30]. This would further enhance the resilience of the coastal community under disaster situations [1].

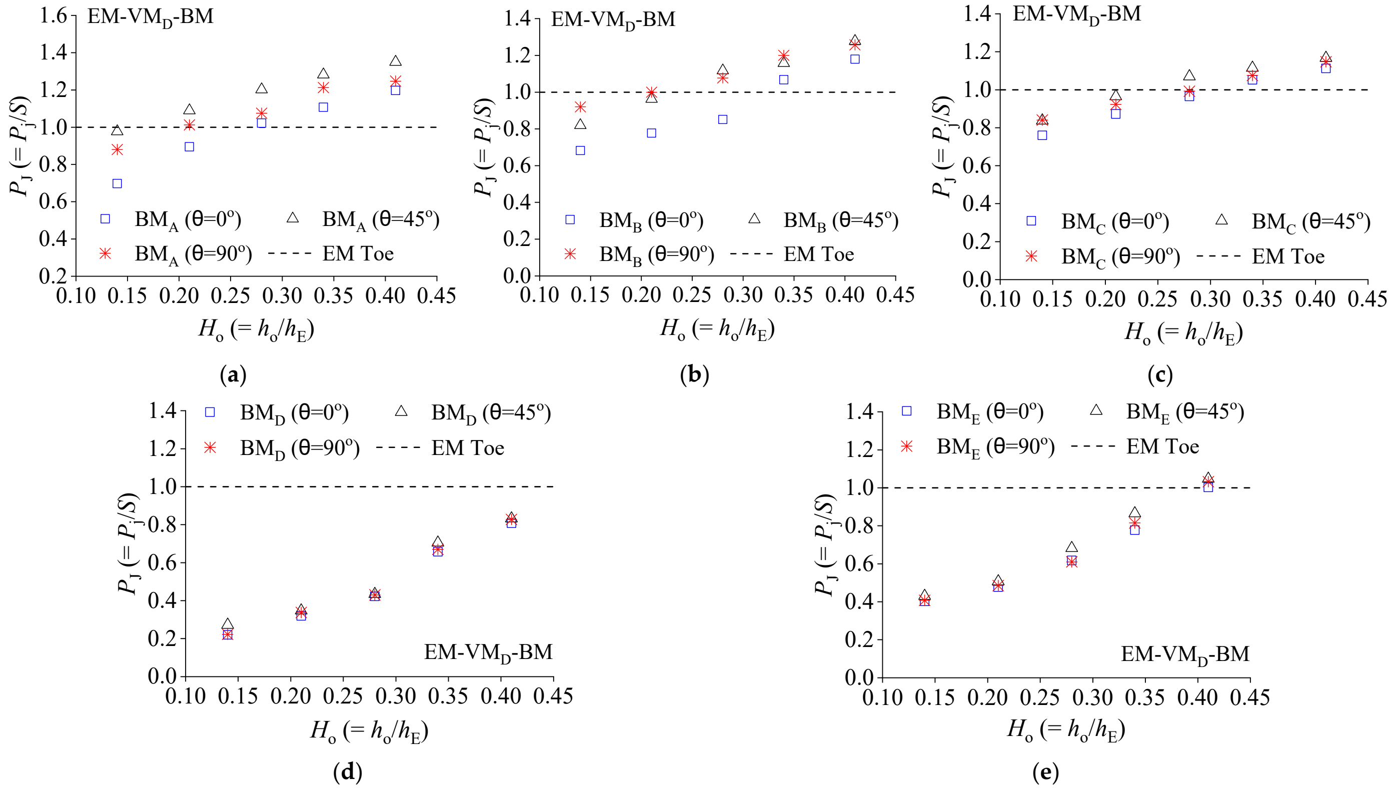

(**a**) (**b**) (**c**)

(**d**) (**e**)

Figure 7. Normalized position of the hydraulic jump P_J (=P_j/S) over the normalized overtopping depth H_o(=h_o/h_E) according to the orientation angle for the experimental case EM-VM$_D$-BM: (**a**) BM$_A$, (**b**) BM$_B$, (**c**) BM$_C$, (**d**) BM$_D$, and (**e**) BM$_E$.

3.4. Force Acting on the Non-Piloti-Type Building Model Under the EM-BM Case Conditions

This section discusses the variation in the tsunami force at the BMs considered in the experimental EM-BM case. The variation in the x-, y-, and z-direction forces on the BMs concerning the non-dimensional overtopping depth are shown in Figure 8 for both the non-piloti-type BMs. As shown in Figure 8, for the BM$_A$, the force on the building in three directions (F_X, F_Y, and F_Z) was higher than the other two non-piloti-type BMs, BM$_B$ and BM$_C$. As shown in Figure 8, the recorded forces of F_X, F_Y, and F_Z are proportional to the rotational angle (θ) due to the decreased and increased effective area concerning the total porosity of the BM (η_{tot}) [7,16,17]. According to the field observations and damages of the existing tsunamis mentioned by Fraser et al. [31] and Ruangrassamee et al. [14], when the buildings are fully enclosed, the lift force (F_Z) becomes more critical than the drag forces (F_X and F_Y), which were similar to the observations of the present study. This is because the pressure difference (static and dynamic pressure) acting on the front and back faces of the BM plays a vital role, even if the flow cannot dissipate quickly enough with respect to the overtopping depth. This phenomenon leads to an uplift in the BM while increasing drag forces F_X and F_Y due to the partial reflections from the adjacent structures, which are represented by the side walls of the experimental flume [16,17]. Even when the BM has a specific porosity, the lift force (F_Z) might be higher due to the turbulence of the flow inside the building structure, like the observations of the present experiment, as mentioned by Fraser et al. [31] and Ruangrassamee et al. [14] (see Figure 8 for BM$_B$ and BM$_C$).

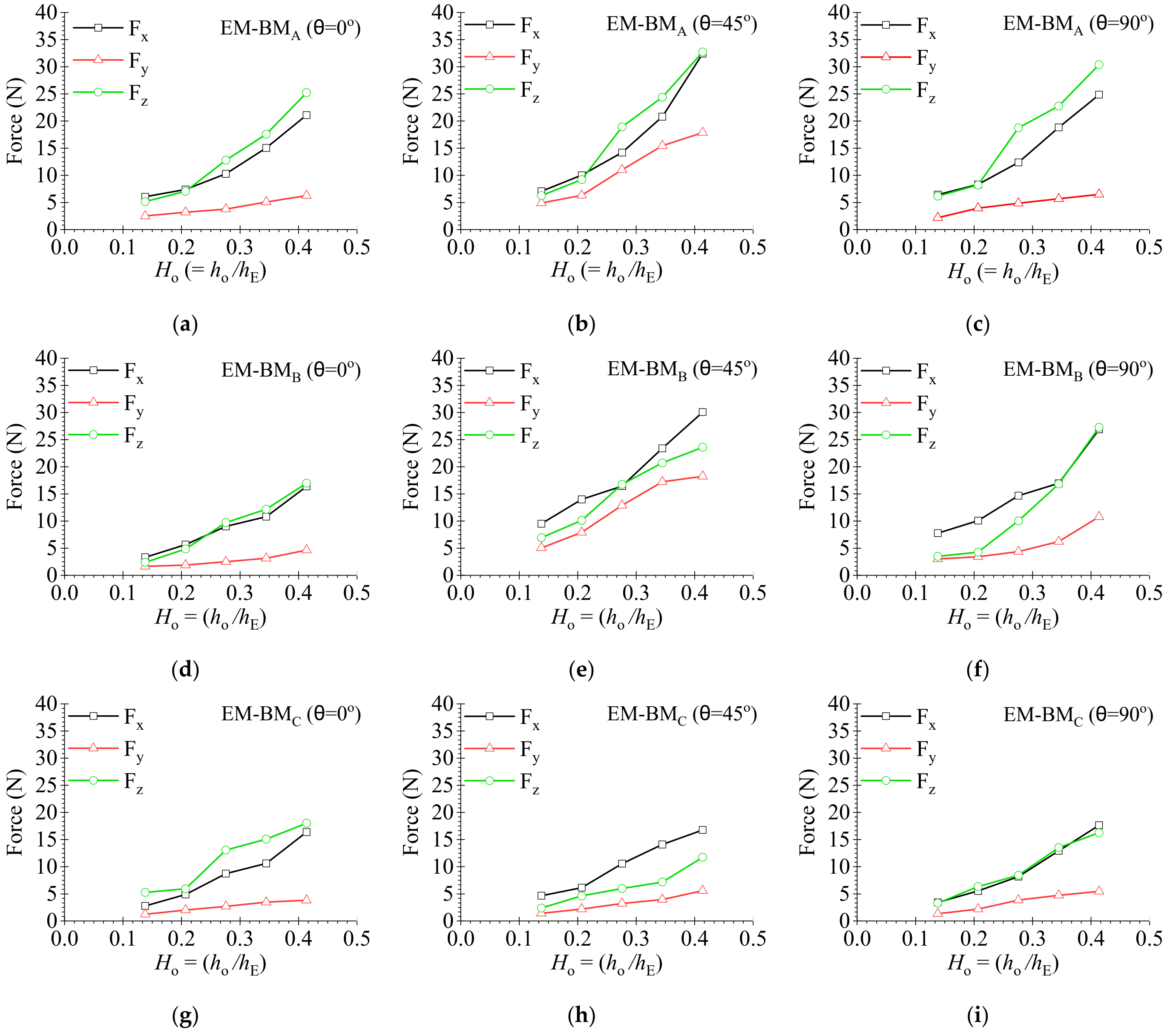

(**a**) (**b**) (**c**)

(**d**) (**e**) (**f**)

(**g**) (**h**) (**i**)

Figure 8. Force acting on the non-piloti-type BM due to the tsunami overtopping flow under the EM-BM case with different orientation angle (θ), where the subscripts A, B, and C denote the building model type: (**a**) EM-BM$_A$ (θ = 0°), (**b**) EM-BM$_A$ (θ = 45°), (**c**) EM-BM$_A$ (θ = 90°), (**d**) EM-BM$_B$ (θ = 0°), (**e**) EM-BM$_B$ (θ = 45°), (**f**) EM-BM$_B$ (θ = 90°), (**g**) EM-BM$_C$ (θ = 0°), (**h**) EM-BM$_C$ (θ = 45°), and (**i**) EM-BM$_C$ (θ = 90°).

Furthermore, forces acting on the piloti-type BMs (BM$_D$ and BM$_E$) are shown in Figure 9 by the rotation angle (θ) for the experimental EM-BM case. For the piloti-type BMs, the z-direction force F_Z (uplift force) was prioritized over the x- and y-directional forces due to the wall-jet-like flow phenomenon observed along the front surface of the piloti column pillars below the BM. In addition, when increasing the overtopping depth, the uplift force F_Z increased gradually except for the BM$_E$ when it was rotated at a 45° angle, as shown in Figure 9. Moreover, with less number of piloti column pillars, the lifted wall-jet-like bow wave along the surface of the piloti-pillar tended to travel along the bottom ceiling level and an increase in the overtopping depth was observed [16].

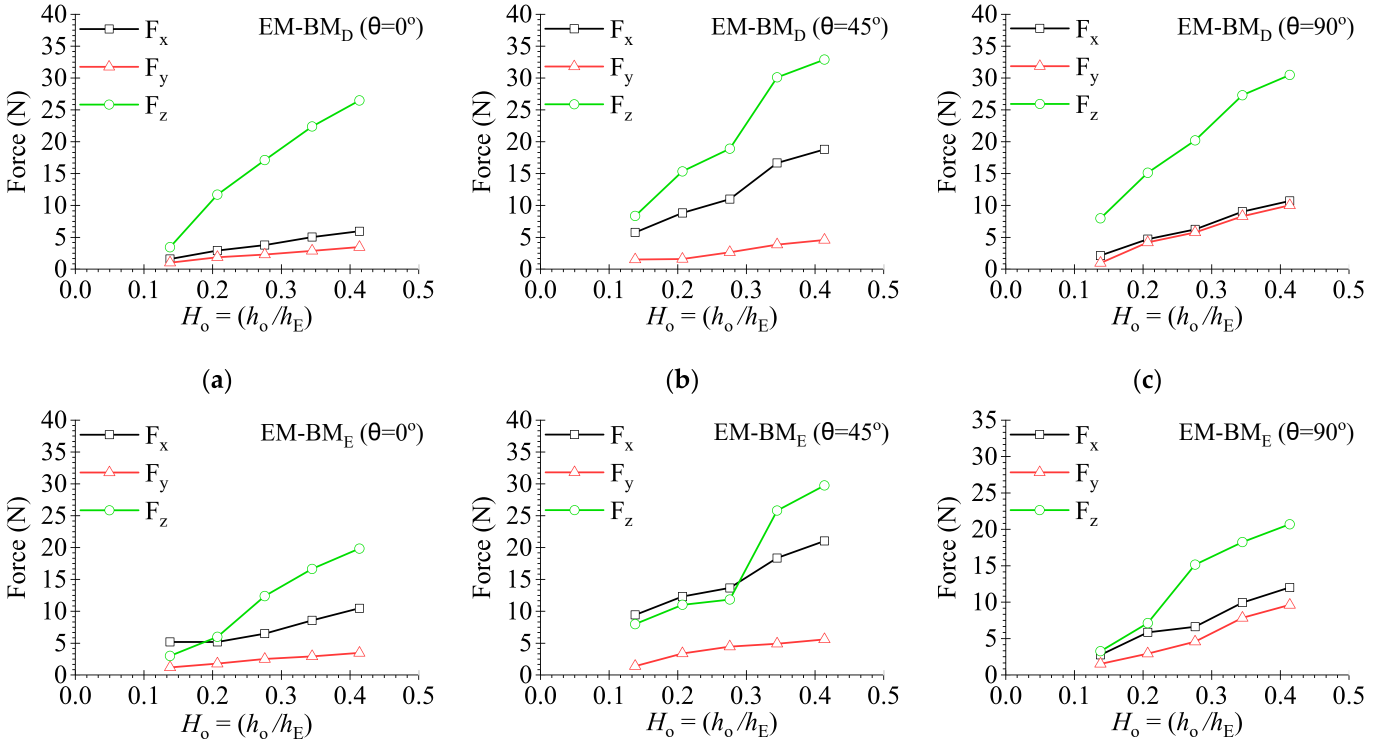

(**a**) (**b**) (**c**)

(**d**) (**e**) (**f**)

Figure 9. Tsunami force acting on the piloti-type BM due to the tsunami overtopping flow following an EM with a different orientation angle (θ) under the EM-BM case conditions, where EM-BM is an embankment model following a building model, and subscripts D and E denote the building model notation: (**a**) EM-BM$_D$ (θ = 0°), (**b**) EM-BM$_D$ (θ = 45°), (**c**) EM-BM$_D$ (θ = 90°), (**d**) EM-BM$_E$ (θ = 0°), (**e**) EM-BM$_E$ (θ = 45°), and (**f**) EM-BM$_E$ (θ = 90°).

This phenomenon further increased the lift force (F_Z) over the BM$_D$, as shown in Figure 9a–c. However, when the number of piloti column pillars like in the BM$_E$ model increased, it disturbed the traveling of the elevated wall-jet bow wave along the ceiling level. As a result, it reduces the lift force (F_Z), as shown in Figure 9d–f. Furthermore, when the piloti-type BMs were rotated, the number of piloti-pillars exposed to the water flow increased. In this situation, the drag force (F_X) and the lift force (F_Z) increased, as shown in Figure 9b,e, respectively [16,17]. Furthermore, when the porosity (η_{tot}) of the non-piloti-type BMs was increased, under the EM-BM case, the force at the BM reduced in relation to the overtopping depth, except for the BM$_B$ when the b_B/W ratios were equal to 0.43 and 0.51, as shown in Figure 8e,f. This is due to the flow interaction and the energy transition of the flow at the BM due to its rotation against the incoming overtopping tsunami flow current concerning the increased effective area of the BM$_B$. Furthermore, when the BM$_C$ was rotated, it increased the porosity further than its frontal condition, which reduced the drag characteristics further, as shown in Figure 8h,i.

3.5. Numerical Model Sensitivity and the Turbulence Intensity at Non-Piloti-Type BM

Figure 10 shows the numerically produced streamlined pattern of the turbulent intensity around the BM$_B$ when it was rotated at 45° and 95° angles, respectively. As shown in Figure 10, when a building structure like BM$_B$ and BM$_C$ faces a tsunami flow current overtopping from an EM, the incoming flow enters the BM through its opening on the frame and exits; increasing the overtopping depth, the velocity of the flow through the BM increases proportionally. This phenomenon increases the fluid circulation inside the BM due to the turbulence characteristics of the flow and provides resistance by the geometric shape of the BM. Due to the fluid circulation inside BM$_B$, the tsunami force increases compared to other non-piloti-type buildings like BM_C, which have an opening in their outer frame from four sides. Snapshots taken during the experiment are shown in Figure S4 in the Supplementary Figures. The steel plate on the BM is used to make a solid placement that avoids movement due to the overtopping flow after removing the load cell fixing arrangement. Figure S4 in the Supplementary Figures depicts the formation conditions of the detached hydraulic jump with a bow wave (see Figure S4a) and Type-1 hydraulic jump (see Figure S4b,c) by BM orientation.

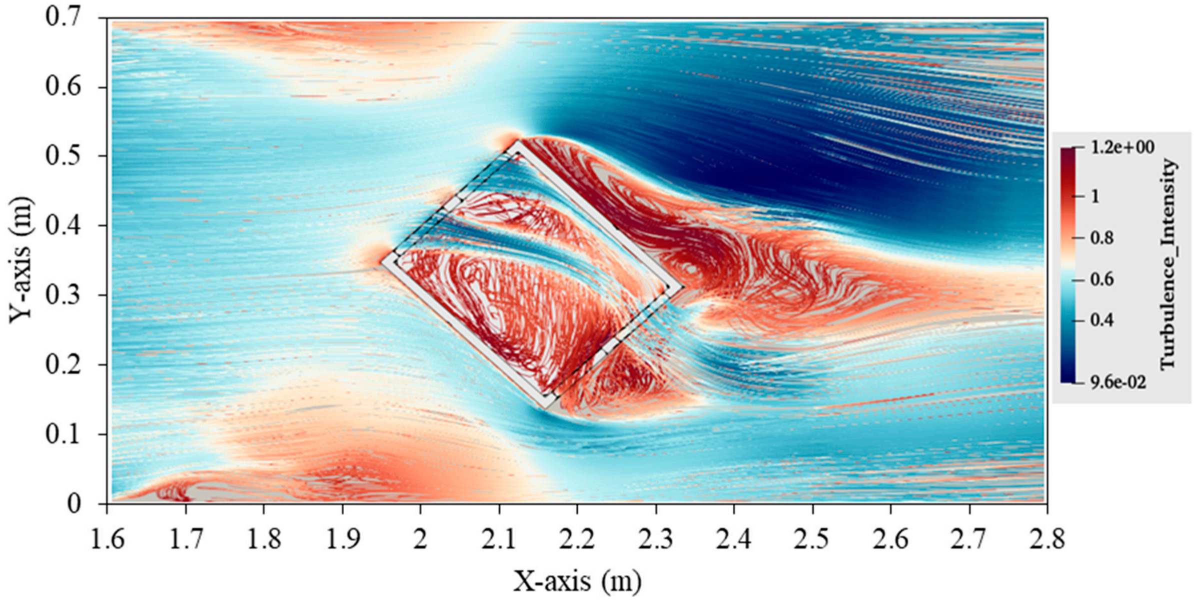

(**a**)

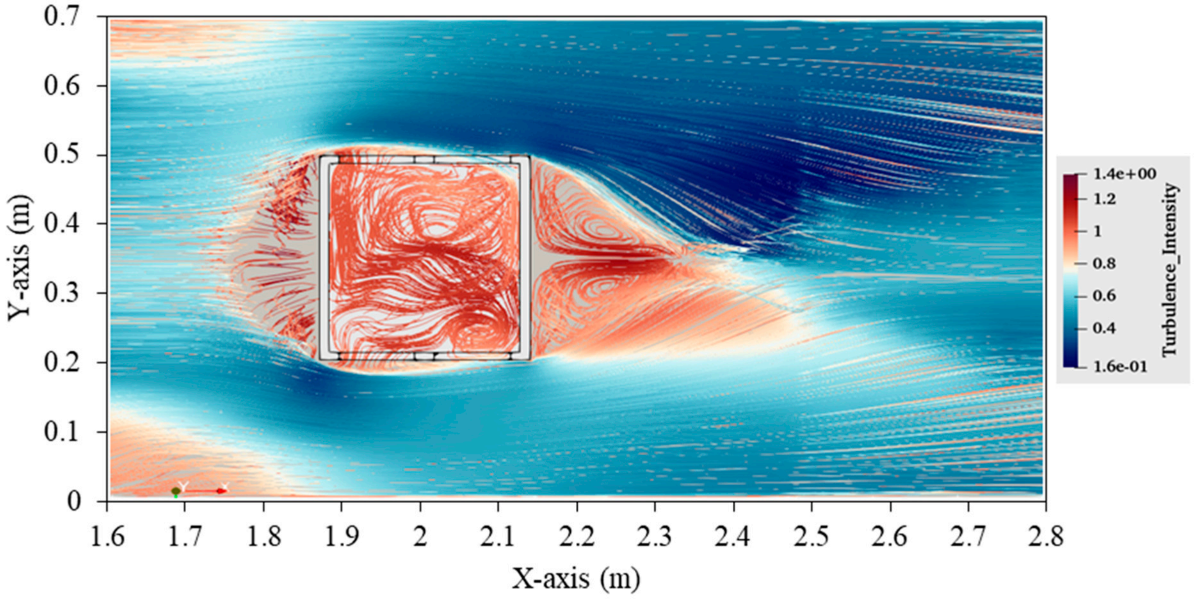

(**b**)

Figure 10. Schematic of the streamlined path around BM_B and BM_C: (**a**) BM_B with a 90° rotation, and (**b**) BM_B with a 45° rotation.

3.6. Tsunami Force Reduction at the Building Model According to the Experimental Setup

As shown in Figure 2, the present experimental study considered three alternative settings to check the overtopping tsunami force reduction and its variability concerning the experimental arrangement and the BM's orientation. Case EM-BM was used as a reference case for the comparison in this section. Figure 11 shows the force reduction in F_X, F_Y, and F_Z for all the non-piloti-type BMs (BM_A, BM_B, and BM_C) related to the non-dimensional overtopping depth H_o ($= h_o/h_E$) when the BM rotation angle (θ) equals to 0°. Depending on the layout of the experimental arrangement and the geometric features of the BM, the overtopping tsunami flow from an embankment could approach the building from a different direction concerning the orientation of the BM. Recent tsunami damage to the structures was observed, and the extent of the damage varied depending on the direction of the approaching wave [31].

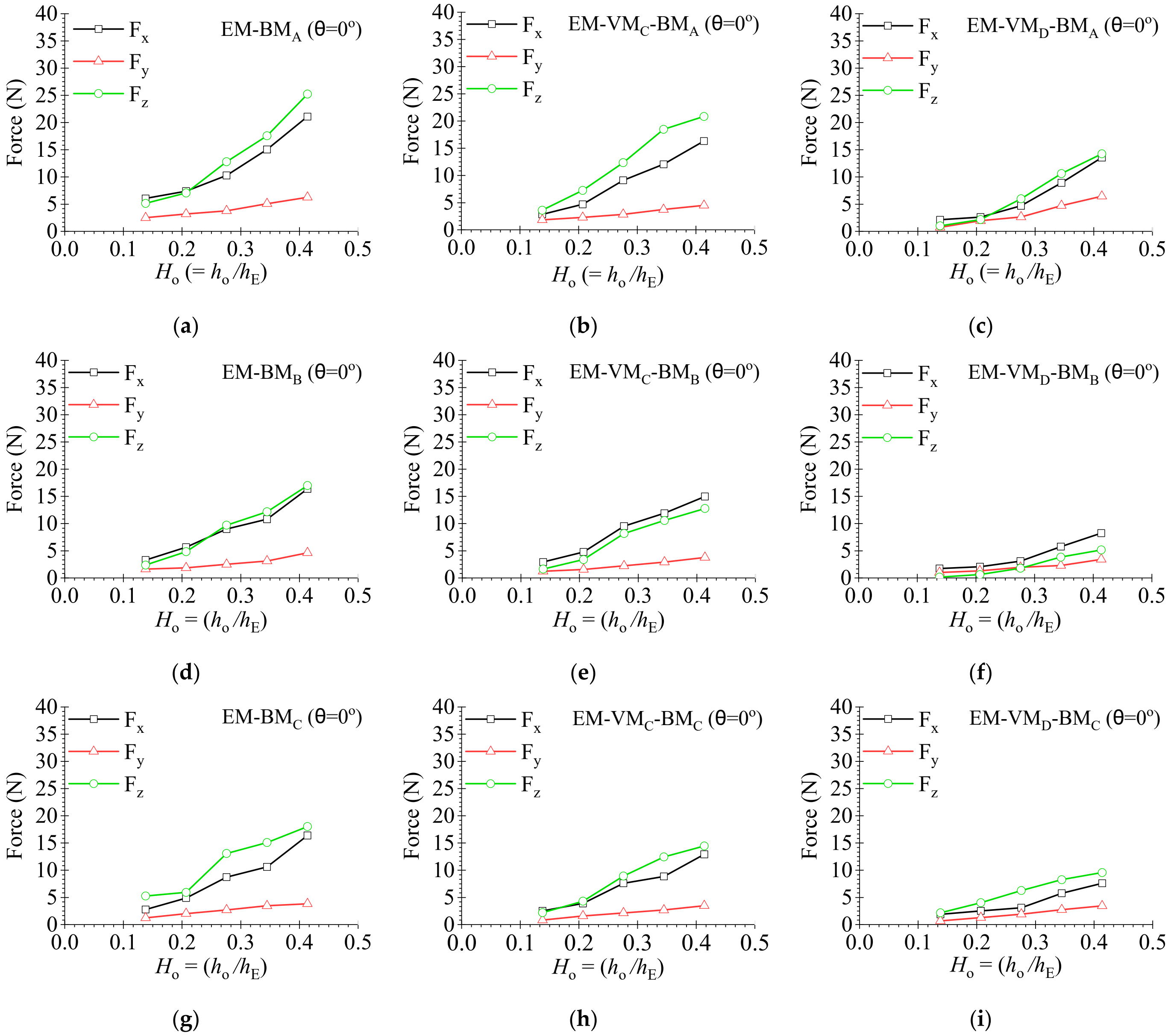

(**a**) (**b**) (**c**)

(**d**) (**e**) (**f**)

(**g**) (**h**) (**i**)

Figure 11. Tsunami force reduction over the non-piloti-type BM by the experimental setup for the $\theta = 0^\circ$ orientation ($b_B/W = 0.35$), the subscripts A, B, and C with the BM denote the building model type, and the subscripts C and D with the VM represent the vegetation model location: (**a**) EM-BM_A ($\theta = 0^\circ$), (**b**) EM-VM_C-BM_A ($\theta = 0^\circ$), (**c**) EM-VM_D-BM_A ($\theta = 0^\circ$), (**d**) EM-BM_B ($\theta = 0^\circ$), (**e**) EM-VM_C-BM_B ($\theta = 0^\circ$), (**f**) EM-VM_D-BM_B ($\theta = 0^\circ$), (**g**) EM-BM_C ($\theta = 0^\circ$), (**h**) EM-VM_C-BM_C ($\theta = 0^\circ$), and (**i**) EM-VM_D-BM_C ($\theta = 0^\circ$).

The most effective method for tsunami force reduction was the utilization of the VM within the gap region (EM-VM_D-BM case) of the EM and BM (see Figure 2c) as an additional alternative approach for the primary defense measures. In addition, when the BM had enough outer frame opening, the reduction in the tsunami force at the BM was high if the vegetation could grow after the first defensive measure, as shown in Figure 11, which would be an added advantage to minimize the total structure failures (toppling, overturning or collapsing) and reduce the rebuilding cost when necessary [17].

Moreover, for the piloti-type BMs (BM_D and BM_E), the tsunami force at the BM would be significantly reduced according to the experimental arrangement, as shown in Figure 12. The pressure introduced by the turbulent intensities in front of the non-piloti-type BM directly influenced the structure and increased the overtopping depth. Furthermore, under the experimental case EM-VM_D-BM conditions (for details, see Figure 2c), the turbulent intensities were ineffective beyond the VM when remaining in the gap region. Behind the VM within the gap region, the static pressure head of the flow transferred as the tsunami force was over the BM, with a low-velocity head due to the absorbance of turbulence lowering the dynamic pressure head. Due to the VM in the gap region under the experimental EM-VM_D-BM case, the force at the non-piloti-type and piloti-type BMs was drastically reduced (see Figures 11 and 12). The percentage reductions in the drag force in the x-direction (F_X) at the BM under the EM-VM_D-BM case conditions ranged between 7.1 and 80.1%, 21.7 and 92.9%, 9.9 and 64.4%, 36.5 and 89.1%, and 47.1 and 77.5% for the BM_A, BM_B, BM_C, BM_D, and BM_E, respectively. Furthermore, the physical configuration of the BM_D and BM_E, which consisted of a series of circular shape cylindrical pillars with significant space, enabled the tsunami overtopping flow current to flow underneath the BM with minimal disruption due to its less effective area, as shown in Figure 12 [16].

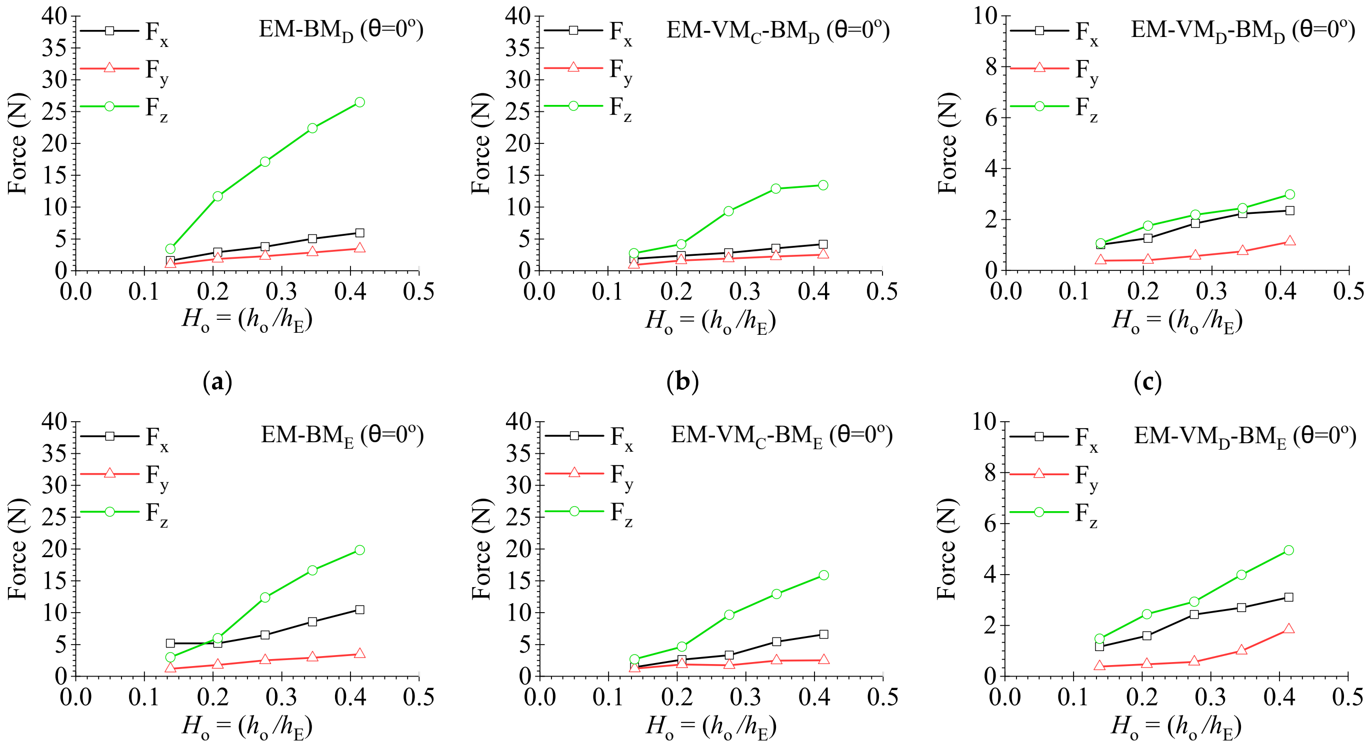

(**a**) (**b**) (**c**)

(**d**) (**e**) (**f**)

Figure 12. Tsunami force reduction over the piloti-type BM concerning the experimental setup for the $\theta = 0^\circ$ orientation ($b_B/W = 0.35$), the subscripts D and E with the BM denote the building model type, and the subscripts C and D with the VM represent the vegetation model location: (**a**) EM-BM_D ($\theta = 0^\circ$), (**b**) EM-VM_C-BM_D ($\theta = 0^\circ$), (**c**) EM-VM_D-BM_D ($\theta = 0^\circ$), (**d**) EM-BM_E ($\theta = 0^\circ$), (**e**) EM-VM_C-BM_E ($\theta = 0^\circ$), and (**f**) EM-VM_D-BM_E ($\theta = 0^\circ$).

3.7. Variation in the Resistance Coefficient (C_R) and Flow Depth Difference on the Non-Piloti-Type Building Model Accoding to the Experimental Setup

During the experiment, the difference in the flow depth reduction between the upstream and downstream of the BM was observed when the overtopping flow reached the BM in relation to its total (η_{tot}) porosity and the experimental layout. This phenomenon led to a reduction in the drag characteristics of the tsunami force at the BM while increasing the overtopping depth from the EM. The supercritical overtopping flow from the EM might maintain the supercritical condition or become subcritical depending on the experimental arrangement, BM orientation, or porosity [16,17]. The drag force became severe with the bluntness, and it was primarily reduced over the piloti-type buildings due to the circular cylindrical shape of the pillars used in this present experiment, as suggested by Dissanayaka and Tanaka [8].

Therefore, it is crucial to define the relationship between the front and back water depth reduction and the choked flow condition due to the drag related to the experimental setup, orientation of BM, and porosity for the non-piloti-type BMs. For evaluating the drag characteristics of the non-piloti-type building models, the $\mathrm{BM_A}$ model in the EM-BM arrangement was selected as the base case. The empirical drag coefficient C_D was defined over the non-piloti-type BMs with the upstream Froude number as a function of the blockage ratio (b_B/W), which assumed that the flow depths of the front and back of the BM was $h_{\mathrm{FB}} \approx h_{\mathrm{BB}}$ as defined by Wüthrich et al. [17] for the post-tsunami overland flows. For the present experimental study $h_{\mathrm{FB}} \gg h_{\mathrm{BB}}$ and the difference in the flow depths upstream and downstream became noticeable by the porosity of the non-piloti-type BM and their orientation. Moreover, due to the steady-state flow conditions used in the present experiment, the chocked characteristics of the flow at the BM were observed [17,32]. Hence, the empirical drag coefficient ($\mathrm{C_D}$) was replaced by the resistance coefficient ($\mathrm{C_R}$). Referring to Equations (5) and (6) the resistance coefficient (C_R) was calculated. For the fully impervious building model ($\mathrm{BM_A}$), the total porosity (η_{tot}) was equal to zero, and the porosity coefficient Φ equalled one. Equation (6) calculated the percentage of the porosity of the $\mathrm{BM_B}$ and $\mathrm{BM_C}$ which were equal to 16.6% and 35.9%, respectively.

The maximum water depth in front of the BM was observed for the EM-BM case; however, for the EM-VMC-BM case, the water depth in front of the BM decreased with increasing velocity. Meantime, when the VM was present at the gap region, the velocity was further lowered in front of the BM, even when the BM was impervious or not, due to the reduced turbulence by the VM. Therefore, the resistance coefficient ($\mathrm{C_{R,0}}$) was calculated for the $\mathrm{BM_A}$ and plotted over the initial Froude number (Fr_o), as shown in Figure 13. Moreover, the resistance coefficient $C_{\mathrm{R,0}}$ for the impervious $\mathrm{BM_A}$ varied between 4.0 and 1.5, 1.9 and 0.9, and 2.9 and 1.2 for the EM-BM, EM-$\mathrm{VM_C}$-BM, and EM-$\mathrm{VM_D}$-BM cases, respectively, for all the rotations (θ) considered in relation to the experimental layout, as shown in Figure 13. These values were higher than those recommended by the ASCE-7 [33] for the post-tsunami overland subcritical flow conditions in front of the impervious BM. However, the values of $C_{\mathrm{R,0}}$ were consistent with the finding of Qi et al. [32] for flows with similar features and varying blockage ratios.

Figure 14 represents the relationship of the non-dimensional difference in water depth [$(h_{\mathrm{BF}} - h_{\mathrm{BB}}/h_o)$] of upstream and downstream of the BM over the H_o when the rotation angle $\theta = 0^{\circ}$ for the $b_B/W = 0.36$, for all the non-piloti-type BMs considered. Moreover, Figure 14a represents the variation in the resistance coefficient ($\mathrm{C_{R,0}}$) with the non-dimensional overtopping depth (H_o) for the $\mathrm{BM_A}$ as an inset figure. Furthermore, for the $\mathrm{BM_B}$ and $\mathrm{BM_{C,}}$ the normalized resistance coefficient $C_R/C_{\mathrm{R,0}}$ are illustrated in Figure 14b,c, according to the experimental arrangement. As shown in Figure 14, with the imperviousness of the BM, the difference in the non-dimensional upstream to the downstream water depth at the BM increased with increasing resistance coefficient, as shown in Figure 14a. Furthermore, when increasing the porosity of the BM, the difference in the non-dimensional from upstream to downstream water depth ratio was reduced while reducing the relative resistance coefficient ($\mathrm{C_R/C_{R,0}}$) for the $\mathrm{BM_B}$ and $\mathrm{BM_C}$, as shown in Figure 14b,c. This makes it possible of reducing the overtopping tsunami force acting on the BM in relation to the increased percentage of the total porosity in the BM frame. The overall consistency of the results shown in Figure 14 shows that when the frontal porosity predominated, the flow passing through the building (regardless of its orientation) was essential in determining the resistance coefficient [16,17]. This figure revealed a higher influence on the resistance coefficient reduction for the configurations with a BM_C, which had larger openings on the outer frame (see Figure 2f). Moreover, for the BM_C with the VM in the EM-VM_D-BM arrangement, it was the most effective solution under the non-piloti-type building category in force reduction due to tsunami overtopping flow from the EM, as shown in Figure 14c.

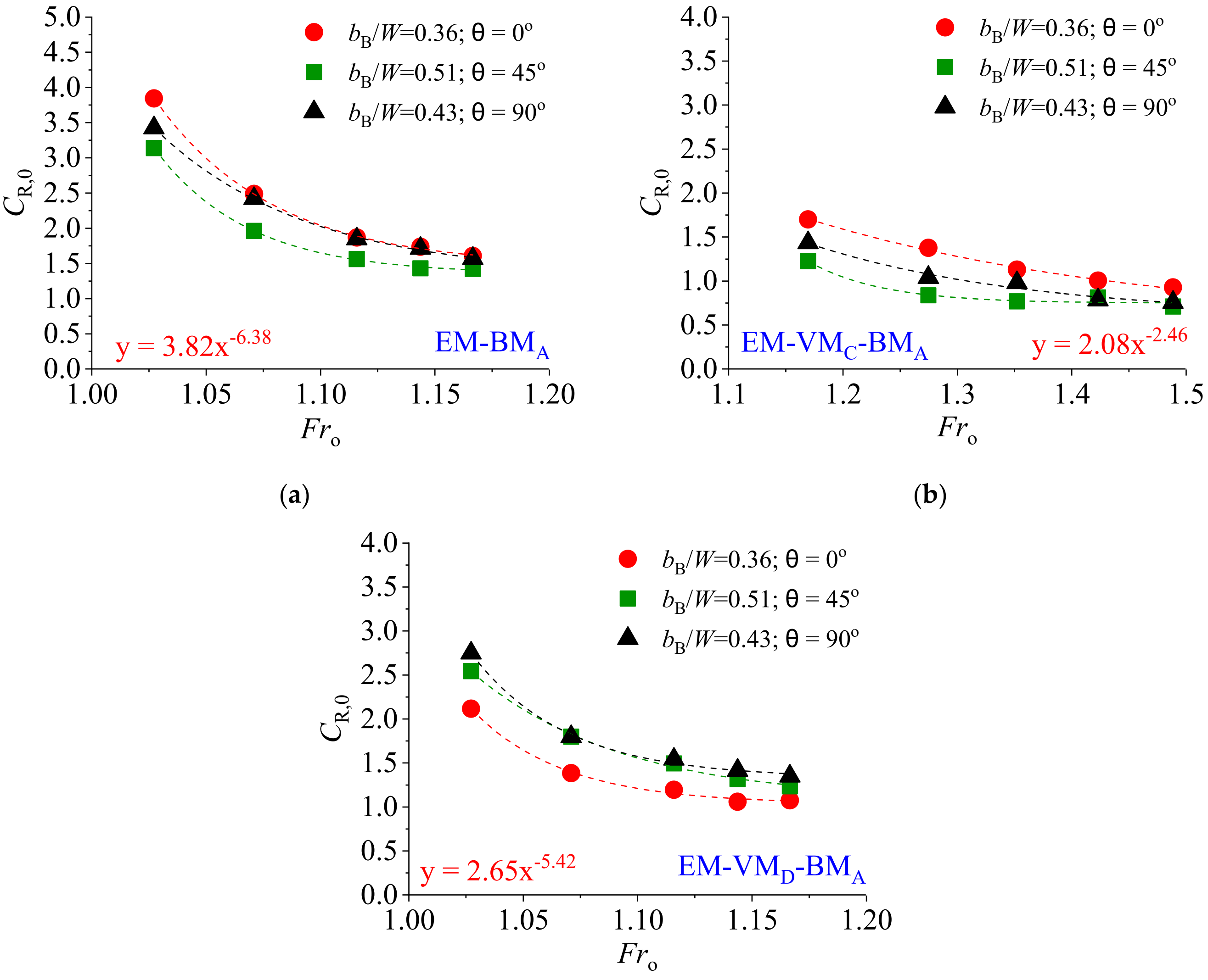

(**a**)

(**b**)

(**c**)

Figure 13. Variation in the resistance coefficient ($C_{R,0}$) at BM_A over the approaching flow Froude number (Fr_o) measured at the EM crest under EM-BM case: (**a**) EM-BM, (**b**) EM-VM_C-BM, and (**c**) EM-VM_D-BM.

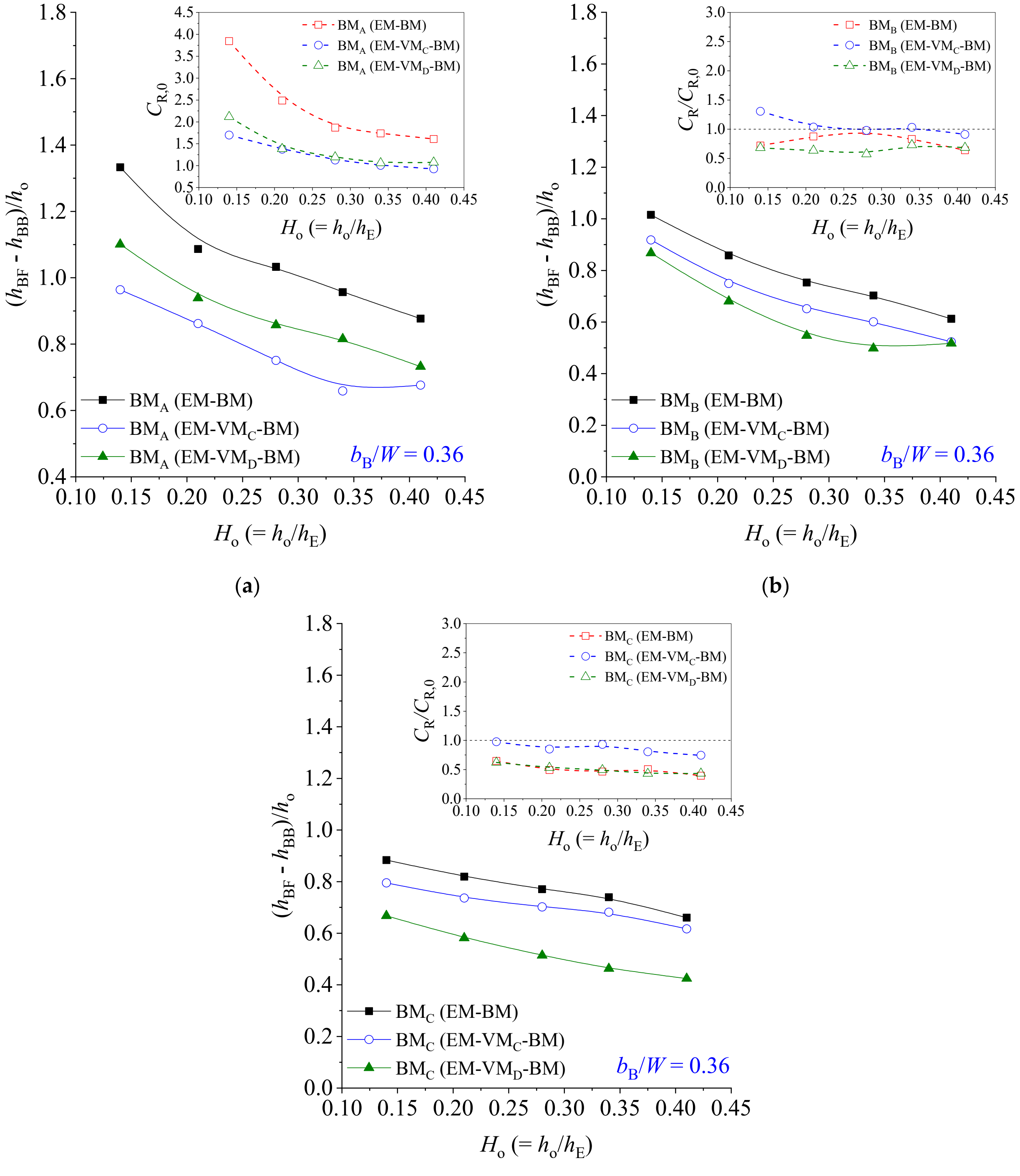

(**a**) (**b**)

(**c**)

Figure 14. Variation in the normalized difference in the upstream and downstream water depth $(h_{BF} - h_{BB})/h_o$ at the building model with the normalized overtopping depth $H_o(= h_o/h_E)$ and the inset figure showing the corresponding resistance coefficient ($C_{R,0}$ or $C_R/C_{R,0}$) with the normalized overtopping depth: (**a**) BM$_A$, (**b**) BM$_B$, and (**c**) BM$_C$.

4. Discussion

4.1. Selection of the Experiment Scale, Vegetation Model, Flow Conditions, Experiment Trials, and the Uncertainties

To select the scale of the experiment, we referred to the existing tsunami records in Sri Lanka in the aftermath of the 2004 IOT, as explained by Goff et al. [20]. Based on the historical tsunami flow depth records, the location in Dickwella City, Matara District, Sri Lanka, has been selected to justify the experiment scale by using the remote sensing application called QGiS, as shown in Figure 1. Furthermore, considering the future tsunami risk assessment and the future mitigation plans suggested by Parape et al. [34], an embankment model (EM) has been used as a primary mitigation measure, as denoted in Figure 2. Furthermore, the VM has been selected as a secondary defensive measure according to the future coastal environmental strategy of Sri Lanka and Japan [19]. The selected VM is represented by the dune trees of *C. equisetifolia* and *P. odoratissimus*. The geometric characteristics of the selected VM are represented by the vertical circular cylinders with a high vegetation thickness of dn equal to 380 No.cm due to the difficulties of making the emergent root systems of *P. odoratissimus* into such an experiment scale for the present study.

According to Mori et al. [35,36], the average diameter of the emergent tree of the *C. equisetifolia* and *P. odoratissimus* ranges between 0.02 m and 0.08 m maximum on the field scale. If we utilized this in the present experiment, the diameter of the emergent tree of *P. odoratissimus* becomes 0.4 to 1.6 mm according to the selected scale. This arrangement would not be effective with the present experiment conditions and the scale selected. Therefore, utilizing a higher tree density to make the vegetation model would be the solution, according to the method described by Tanaka [2]. In addition, the selected scale, as shown in Figure 2e, three-rotational angles (θ) (or b_B/W ratios) of the BM have been selected that are suited for the experiment. This experiment used a steady-state overtopping flow from the EM to evaluate the post-tsunami force transition at the BM [7,17]. Moreover, each experiment trial lasted for nearly six minutes to achieve the required measurements while securing the steady-state flow conditions, and for each case, three trials were conducted to keep the uncertainty of the force gauge reading less than 5.0% [17,22].

4.2. Numerical Model Calibration, Validation and Turbulence Intensity

According to the numerical model developed and calibrated, the selected turbulence model captured the flow behavior within the domain (see Figure S3 in the Supplementary Figures) [24,37–39]. The statistical indices selected explain the accuracy of the numerical prediction, as listed in Table 2. Furthermore, the selected mesh and the turbulence model of k–ω SST captured the abrupt changes in flow after overtopping from the EM, as shown in Figure S3 of Supplementary Figures [23,37,38]. Due to the geometric characteristics of the BM_B, the developed vortex regime inside the BM further increased its instability, as shown in Figure 10, while increasing the force. This would be reduced by utilizing a four-sided opening structure or an elevated building structure like BM_D or BM_E. However, in real-scale applications, buildings like warehouses fall into this category, with limited opening spaces related to their serviceability. Hence, identifying the turbulence characteristics would be important to strengthen the building structures and minimize the damage under disastrous situations. As mentioned by Manwasekara et al. [16] and Wüthrich et al. [17], the concave shapes of the building structures increase the drag force during tsunamis or floods, leading to an ultimate disaster if the structure cannot withstand the force. Therefore, the developed numerical model could be applied for further evaluation in the future.

4.3. Flow Structure and the Hydraulic Jump Formation

As shown in Figure 4, the tsunami flow after overtopping from the EM converts to a subcritical flow or supercritical flow in front of the BM considering the BM total porosity (η_{tot}), BM orientation (θ or b_B/W ratio), and the experimental arrangement (see Figure 2a–c). The variations in the tsunami force at the building model are significant to the flow structure in front of the BM concerning the experimental layout and the chocked characteristics of the overtopping flow [17].

In addition, the flow structure at the BM was similar to the EM-BM and EM-VM_C-BM experimental cases. The only noted difference was the low flow depths and the increased velocities around the BM compared to the EM-BM case. Moreover, for the non-piloti-type BMs, concerning the orientation angle under the experiment case EM-BM, the Type-2 hydraulic jump was observed when increasing the overtopping flow and the ratio of the water depth in front of the BM to the overtopping flow depth ($h_{\mathrm{BE}}/h_{\mathrm{E}}$) was more significant than 0.5, as shown in Figure 5. Furthermore, the observed hydraulic jump transformed to a Type-1 from a Type-2 jump and extended towards the downstream surface of the EM while increasing the overtopping flow from the EM. This was denoted as the non-dimensional hydraulic jump position as shown in Figures 6 and 7, according to the BM orientation (θ), BM total porosity (η_{tot}), and the experimental layout [22,30]. Furthermore, allowing the flow through the BM will omit the formation of a Type-2 hydraulic jump and reduce the force exerted on the BM, which will increase the safety of the primary defensive measure while using piloti-type BMs, as shown in Figure 7. This is because the increased free space below the piloti-type BMs allows free flow with minimum restrictions over the flow while enhancing the safety of associated defensive measures. In contrast, under the EM-VM$_{\mathrm{C}}$-BM case conditions, with the increased bluntness of the BM, the Type-1 jump converted to a Type-2 jump, as shown in Figure 7. Therefore, it is essential to understand the effect of the arrangement of the primary defensive measure, including the BM orientation (θ) and the porosity of the BM (η_{tot}). On the other hand, the building structure design should be capable of handling the flow in front of the BM, including the hydraulic jump type, to increase the safety of dwellings located on the coastline.

4.4. Force Reduction at the Building Model Using the VM

This study primarily investigated the force reduction at the BM following an EM, including a VM with different experimental arrangements, orientations, and geometric conditions of the BM under steady-state flow conditions. Because the majority of the case studies have been conducted for the unsteady flows under the dam-break flow conditions [16] and post-tsunami flow conditions [17]. Hence, the present case study has been carried out to fill the gap of knowledge regarding the tsunami forces at the BM due to the overtopping quasi-steady tsunami flow following a primary and secondary defensive measure. The turbulence characteristics of the overtopping flow from the EM are a primary concern for force transfer at the BM and potential structural failure. This is particularly critical or not when following a primary defensive line, such as an EM, forest, or hybrid defense alternative accordingly BM geometry as shown in Figure 10. The direct exposure to these turbulent flows can significantly impact the stability and integrity of the BM, necessitating careful consideration in the design and implementation of defensive measures [31]. The present research implemented force reduction by utilizing a vegetation model (VM) at the EM crest and the gap region between the EM toe and the BM (for details, see Figure 2) to determine the extent the fluid force can be reduced, as shown in Figures 11 and 12.

The quantitative results of the tsunami force reduction presented in Figures 11 and 12 show the effectiveness of the VM model located in the gap region under the experimental EM-VM$_{\mathrm{D}}$-BM case. This is because the VM in the gap region neutralizes the turbulence characteristics of the overtopping flow downstream of the VM, which were directly proportional to the reduced forces at the BM concerning its total porosity (η_{tot}) and the orientation angle (θ). Furthermore, the resistance coefficient was reduced when the VM was kept in the gap region due to the reduced turbulence characteristics over the non-piloti-type BMs, as shown in Figure 14. Therefore, it is essential to utilize vegetation as a secondary defensive measure while maintaining a primary defensive line to reduce the force exerted on the building structures to mitigate the tsunami risk. In addition, maintaining a proper vegetation density, either single or double-layered, further enhances the coastal community's safety [1].

4.5. Force Reduction at the Building Model Concerning Its Geometric Shapes

In addition, concerning the structural properties discussed in previous studies, the present experiment examined circular-shaped piloti-columns for the piloti-type BMs (BM$_{\mathrm{D}}$ and BM$_{\mathrm{E}}$). These columns reduced the force exerted on the BM by decreasing the effective area exposed to the flow. This design aims to enhance the BM's resilience by minimizing the impact of overtopping flows, as shown in Figures 9 and 12 [16,17]. Moreover, in the present study, due to the limitations in the experimental flume height, the piloti pillars' height was limited, which equals a single floor height of the selected two-story BM. The stability of the building structure, subjected to a tsunami flow interaction, was directly proportional to the concave shapes, building structure orientation, total porosity, and the following primary defensive measures [14]. Referencing the tsunami flow force reduction, the non-piloti-type BMs (BM_A, BM_B, and BM_C) are receiving more attention throughout the entire experiment series than the piloti-type BMs (BM_D and BM_E). Therefore, the drag characteristics of the BM were presented by the resistance coefficient (C_R), which was explained by the developed Equations (1)–(5). Moreover, when the BM is subjected to a tsunami flow interaction, the difference in the upstream and downstream water depths of the BM directly interlinked to the force at the BM, where described by the C_R concerning the porosity of the BM, as shown in Figure 14. If the porosity is high, overtopping flow is allowed to pass through the BM or below the BM due to its geometric characteristics [7,10,16,17]. As shown in Figure 12, it is evident that, with the introduction of piloti-pillar arrangement for the elevated BMs, the force exerted on the BM due to the overtopping tsunami flow is reduced by 20–30% due to the reduced effective area, where tsunami flow interacted than the non-piloti-type BMs. Moreover, introducing the VM model at the downstream gap region, force on the piloti-type BMs has been further reduced by 60–70% compared to the non-piloti-type BMs. Hence, it is vital to know that raising BMs from the ground level by introducing piloti-type pillars as a structural alternative would enhance the safety and strength of the building structure against failure during a catastrophe like a tsunami, river flood, or storm surge.

5. Conclusions

Due to the past recorded tsunami inundation events, a severe impact has been observed on the coastal building structures exposed to the tsunami flow. Many coastal building structures have not survived by collapsing or overturning due to their outer frame porosity and orientation of the effective face interacting with the tsunami flow. Moreover, in some regions where dense forests or forests have grown to a certain thickness, the buildings have survived by breaking or collapsing but have been submerged. Therefore, to ensure the stability of the coastal building structure, it is crucial to identify the force over the building model, which follows a certain defensive measure under different flow characteristics. As a result, the present study's findings can be concluded as follows.

- Under the different flow conditions, the effect of the approaching overtopping flow from a coastal embankment was considered under the EM-BM case, which directly hit the BM and transferred the tsunami force to the BM. This force at the BM would be altered regarding the building model porosity and orientation angle. Moreover, the observed behavior of the formation conditions of the Type-2 hydraulic jump would be further adjusted with BM's orientation and porosity because the Type-2 hydraulic jump might affect the safety of the EM on a prototype scale due to accelerating the erosion of the embankment body.
- For the EM-VM_C-BM case, the flow structure kept the same properties downstream and at the BM when the VM was on the EM crest. This alternative solution further reduced the force at the non-piloti-type BM due to the low flow depths in front of the BM. Furthermore, under the EM-VM_D-BM case conditions, the VM was kept between the gap region of the EM and the BM (see Figure 2c). Under this experimental condition, the VM thickness and density controlled the turbulence effect of the overtopping flow, which contributed to reducing the force at the BM noticeably, including non-piloti and piloti. Therefore, it can be suggested that even the non-piloti-type BM can withstand the tsunami flow force without damage except submergence with a specific porosity.
- The resistance coefficients' calculated values agreed with those from previous experimental investigations for a reference building that was entirely impervious and subject to a frontal flow. Moreover, the present study found that when a fluid flowed through openings of the BM, the difference in flow depths between the upstream and

downstream sides further decreased the horizontal forces. This led to a significant reduction in the resistance coefficient, which was found to be directly proportional to the porosity of the building.

- From all the experimental cases and building models considered concerning the collected data, a piloti-type building model with an increased number of pillars would be the most convenient solution that can survive well over the tsunami force even though the survivability of the piloti-type buildings could be further improved with grown vegetation within the gap region of the building line and the embankment toe. Moreover, in real-world applications, these findings highlight the crucial importance of openings in minimizing the tsunami force imposed by the fluid flow on the non-piloti-type buildings and reducing the depth of inundation, which results in the creation of a safer and more resilient structure in future concerning the different defense approaches will be considered.

Supplementary Materials: The following supporting information can be downloaded at: https://www.mdpi.com/article/10.3390/geosciences14110287/s1, Supplementary notes included general equations utilized in the numerical model, modelling of free surface profiles, turbulence modelling, numerical model stability and time-step control, calculation of turbulence intensity and statistical indicators used to evaluate the numerical model. Figure S1: Numerical model boundary conditions and the mesh refinement region; Figure S2: Comparison of the streamwise velocity profile observed over the crest of the embankment of Objective 3 with experiment (this study) and numerical model with BM_A building model kept in 0° angle rotation concerning the different mesh grid and the turbulence model: (a) Mesh 1, (b) Mesh 2, (c) Mesh 3; Figure S3: Comparison of the numerically predicted free surface profile of the overtopping flow from an embankment with the BM_A building model kept in 0° angle rotation, with the experimental results concerning the mesh and the turbulence model: (a) Mesh 01, (b) Mesh 2, (c) Mesh 3; Snapshots taken during the experiment which show the flow behavior around the BM_B when the non-dimensional overtopping depth was equal (H_o) 0.28; (a) BM_B rotated by 0°, (b) BM_B rotated by 45° and (c) BM_B rotated by 90°; Figure S4: Snapshots taken during the experiment which show the flow behavior around the BM_B when the non-dimensional overtopping depth was equal (H_o) 0.28; (a) BM_B rotated by 0°, (b) BM_B rotated by 45° and (c) BM_B rotated by 90°.

Author Contributions: Conceptualization, methodology, model preparation, experimental investigation, data processing, and analysis, writing—original draft, and visualization: K.D.C.R.D. Conceptualization, resources, writing—review and editing, supervision, project administration, funding acquisition: N.T. All authors have read and agreed to the published version of the manuscript.

Funding: This research received no external funding.

Data Availability Statement: Upon reasonable request, the author can provide the relevant data only for research and development.

Acknowledgments: The authors thank the Japanese Ministry of Education (Monbukagakusho) for their assistance. The authors would like to thank the anonymous reviewers for their constructive remarks, which helped us enhance the quality of the work.

Conflicts of Interest: The authors declare no conflicts of interest.

References

1. Dissanayaka, K.D.C.R.; Tanaka, N.; Vinodh, T.L.C. Integration of Eco-DRR and Hybrid Defense System on Mitigation of Natural Disasters (Tsunami and Coastal Flooding): A Review. *Nat. Hazards* **2021**, *110*, 1–28. [CrossRef]
2. Tanaka, N. Effectiveness and Limitations of Coastal Forest in Large Tsunami: Conditions of Japanese Pine Trees on Coastal Sand Dunes in Tsunami Caused by Great East Japan Earthquake. *J. Jpn. Soc. Civ. Eng. Ser. B1 (Hydraul. Eng.)* **2012**, *68*, II-7–II-15. [CrossRef] [PubMed]
3. Tappin, D.R.; Evans, H.M.; Jordan, C.J.; Richmond, B.; Sugawara, D.; Goto, K. Coastal Changes in the Sendai Area from the Impact of the 2011 Tōhoku-Oki Tsunami: Interpretations of Time Series Satellite Images, Helicopter-Borne Video Footage and Field Observations. *Sediment. Geol.* **2012**, *282*, 151–174. [CrossRef]
4. Zaha, T.; Tanaka, N.; Kimiwada, Y. Flume Experiments on Optimal Arrangement of Hybrid Defense System Comprising an Embankment, Moat, and Emergent Vegetation to Mitigate Inundating Tsunami Current. *Ocean. Eng.* **2019**, *173*, 45–57. [CrossRef]

5. Dissanayaka, K.D.C.R.; Tanaka, N.; Hasan, M.-K. Effect of Orientation and Vegetation over the Embankment Crest for Energy Reduction at Downstream. *Geosciences* **2022**, *12*, 354. [CrossRef]
6. Riviere, N.; Vouaillat, G.; Launay, G.; Mignot, E. Emerging Obstacles in Supercritical Open-Channel Flows: Detached Hydraulic Jump versus Wall-Jet-like Bow Wave. *J. Hydraul. Eng.* **2017**, *143*, 04017011. [CrossRef]
7. Wüthrich, D.; Pfister, M.; Nistor, I.; Schleiss, A.J. Experimental Study on the Hydrodynamic Impact of Tsunami-like Waves against Impervious Free-Standing Buildings. *Coast. Eng. J.* **2018**, *60*, 180–199. [CrossRef]
8. Dissanayaka, K.D.C.R.; Tanaka, N. Comparison of the Flow around Circular and Rectangular Emergent Cylinders with Subcritical and Supercritical Conditions. *Fluids* **2023**, *8*, 124. [CrossRef]
9. Chock, G.; Robertson, I.; Kriebel, D.; Francis, M.; Nistor, I. *Tohoku, Japan, Earthquake and Tsunami of 2011: Performance of Structures under Tsunami Loads*; American Society of Civil Engineers: Reston, VA, USA, 2013; ISBN 978-0-7844-1249-7.
10. Nakano, Y. Structural Design Requirements for Tsunami Evacuation Buildings in Japan. In *SP-313 Proceedings of the First ACI & JCI Joint Seminar: Design of Concrete Structures Against Earthquake and Tsunami Damage*; ACI: Farmington Hills, MI, USA, 2017. [CrossRef]
11. Cox, D.; Tomita, T.; Lynett, P.; Holman, R. Tsunami Inundation with Macro-Roughness in the Constructed Environment. In *Coastal Engineering 2008*; World Scientific Publishing Company: Singapore, 2009; pp. 1421–1432. ISBN 978-981-4277-36-5.
12. Dang-Vu, H.; Shin, J.; Lee, K. Seismic Fragility Assessment of Columns in a Piloti-Type Building Retrofitted with Additional Shear Walls. *Sustainability* **2020**, *12*, 6530. [CrossRef]
13. Lukkunaprasit, P.; Ruangrassamee, A. Tsunami Loading on Buildings with Openings. *Sci. Tsunami Hazards* **2009**, *28*, 303–310.
14. Ruangrassamee, A.; Yanagisawa, H.; Foytong, P.; Lukkunaprasit, P.; Koshimura, S.; Imamura, F. Investigation of Tsunami-Induced Damage and Fragility of Buildings in Thailand after the December 2004 Indian Ocean Tsunami. *Earthq. Spectra* **2006**, *22*, 377–401. [CrossRef]
15. Macabuag, J.; Raby, A.; Pomonis, A.; Nistor, I.; Wilkinson, S.; Rossetto, T. Tsunami Design Procedures for Engineered Buildings: A Critical Review. *Proc. Inst. Civ. Eng.—Civ. Eng.* **2018**, *171*, 166–178. [CrossRef]
16. Manawasekara, C.; Mizutani, N.; Aoki, S. Influence of Openings and Orientation on Tsunami Generated Forces on Buildings. *J. Disaster Res.* **2016**, *11*, 670–679. [CrossRef]
17. Wüthrich, D.; Pfister, M.; Schleiss, A.J. Forces on Buildings with Openings and Orientation in a Steady Post-Tsunami Free-Surface Flow. *Coast. Eng.* **2020**, *161*, 103753. [CrossRef]
18. Chen, C.; Lai, Z.; Beardsley, R.C.; Sasaki, J.; Lin, H.; Ji, R.; Sun, Y. The March 11, 2011 Tōhoku M9.0 Earthquake-Induced Tsunamiand Coastal Inundation along the Japanese Coast: A Model Assessment. *Prog. Oceanogr.* **2014**, *123*, 84–104. [CrossRef]
19. Tanaka, N.; Yasuda, S.; Iimura, K.; Yagisawa, J. Combined Effects of Coastal Forest and Sea Embankment on Reducing the Washout Region of Houses in the Great East Japan Tsunami. *J. Hydro-Environ. Res.* **2014**, *8*, 270–280. [CrossRef]
20. Goff, J.; Liu, P.L.F.; Higman, B.; Morton, R.; Jaffe, B.E.; Fernando, H.; Lynett, P.; Fritz, H.; Synolakis, C.; Fernando, S. Sri Lanka Field Survey after the December 2004 Indian Ocean Tsunami. *Earthq. Spectra* **2006**, *22*, 155–172. [CrossRef]
21. Tanaka, N.; Yagisawa, J.; Yasuda, S. Characteristics of Damage Due to Tsunami Propagation in River Channels and Overflow of Their Embankments in Great East Japan Earthquake. *Int. J. River Basin Manag.* **2012**, *10*, 269–279. [CrossRef]
22. Rashedunnabi, A.H.M.; Tanaka, N. Energy Reduction of a Tsunami Current through a Hybrid Defense System Comprising a Sea Embankment Followed by a Coastal Forest. *Geosciences* **2019**, *9*, 247. [CrossRef]
23. Dissanayaka, K.D.C.R.; Tanaka, N.; Hasan, M.K. Numerical Simulation of Flow over a Coastal Embankment and Validation of the Nappe Flow Impinging Jet. *Model. Earth Syst. Environ.* **2023**, *10*, 777–798. [CrossRef]
24. OpenFOAM User Guide. Available online: https://www.openfoam.com/documentation/user-guide (accessed on 30 January 2024).
25. Karami, H.; Farzin, S.; Badeli, M.; Mousavi, S.F. Analysis of Flow Pattern with Low Reynolds Number around Different Shapes of Bridge Piers, and Determination of Hydrodynamic Forces, Using OpenFOAM Software. *Rehabil. Civ.* **2017**, *6*, 34–48. [CrossRef]
26. Bayon, A.; Toro, J.P.; Bombardelli, F.A.; Matos, J.; López-Jiménez, P.A. Influence of VOF Technique, Turbulence Model and Discretization Scheme on the Numerical Simulation of the Non-Aerated, Skimming Flow in Stepped Spillways. *J. Hydro-Environ. Res.* **2018**, *19*, 137–149. [CrossRef]
27. Hager, W.H. B-Jump in Sloping Channel. *J. Hydraul. Res.* **1988**, *26*, 539–558. [CrossRef]
28. Imanian, H.; Mohammadian, A. Numerical Simulation of Flow over Ogee Crested Spillways under High Hydraulic Head Ratio. *Eng. Appl. Comput. Fluid Mech.* **2019**, *13*, 983–1000. [CrossRef]
29. Imanian, H.; Mohammadian, A.; Hoshyar, P. Experimental and Numerical Study of Flow over a Broad-Crested Weir under Different Hydraulic Head Ratios. *Flow Meas. Instrum.* **2021**, *80*, 102004. [CrossRef]
30. Rahman, M.-A.; Tanaka, N.; Rashedunnabi, A.H.M. Flume Experiments on Flow Analysis and Energy Reduction through a Compound Tsunami Mitigation System with a Seaward Embankment and Landward Vegetation over a Mound. *Geosciences* **2021**, *11*, 90. [CrossRef]
31. Fraser, S.; Raby, A.; Pomonis, A.; Goda, K.; Chian, S.C.; Macabuag, J.; Offord, M.; Saito, K.; Sammonds, P. Tsunami Damage to Coastal Defences and Buildings in the March 11th 2011 Mw9.0 Great East Japan Earthquake and Tsunami. *Bull. Earthq. Eng.* **2013**, *11*, 205–239. [CrossRef]
32. Qi, Z.X.; Eames, I.; Johnson, E.R. Force Acting on a Square Cylinder Fixed in a Free-Surface Channel Flow. *J. Fluid Mech.* **2014**, *756*, 716–727. [CrossRef]

33. *ASCE/SEI 7-10*; ASCE-7 Minimum Design Loads for Buildings and Other Structures; Commentary for Chapters C11-C22 (Seismic). Structural Engineering Institute, American Society of Civil Engineers: Reston, VA, USA, 2013.
34. Parape, C.D.; Premachandra, C.; Tamura, M.; Bari, A.; Disanayake, R.; Welikanna, D.; Jin, S.; Sugiura, M. Building Damage and Business Continuity Management in the Event of Natural Hazards: Case Study of the 2004 Tsunami in Sri Lanka. *Sustainability* **2013**, *5*, 456–477. [CrossRef]
35. Mori, N.; Chang, C.-W.; Inoue, T.; Akaji, Y.; Hinokidani, K.; Baba, S.; Takagi, M.; Mori, S.; Koike, H.; Miyauchi, M.; et al. Parameterization of Mangrove Root Structure of *Rhizophora stylosa* in Coastal Hydrodynamic Model. *Front. Built Environ.* **2022**, *7*, 782219. [CrossRef]
36. Mori, N.; Imamura, F. The 2011 Tohoku Earthquake Tsunami Joint Survey Group Nationwide Post Tsunami Event Survey and Analysis of the 2011 Tohoku Earthquake Tsunami. *Coast. Eng.* **2011**, *54*, 1250001-1–1250001-27. [CrossRef]
37. Daneshfaraz, R.; Minaei, O.; Abraham, J.; Dadashi, S.; Ghaderi, A. 3-D Numerical Simulation of Water Flow over a Broad-Crested Weir with Openings. *ISH J. Hydraul. Eng.* **2021**, *27*, 88–96. [CrossRef]
38. Daneshfaraz, R.; Dasineh, M.; Ghaderi, A.; Sadeghfam, S. Numerical Modeling of Hydraulic Properties of Sloped Broad Crested Weir. *AUT J. Civ. Eng.* **2019**, *4*, 229–240. [CrossRef]
39. Fereshtehpour, M.; Chamani, M.R. Numerical and Experimental Modeling of Flow over Drop with Upstream Circular Channel. *Sharif J. Civ. Eng.* **2021**, *362*, 101–109.

Disclaimer/Publisher's Note: The statements, opinions and data contained in all publications are solely those of the individual author(s) and contributor(s) and not of MDPI and/or the editor(s). MDPI and/or the editor(s) disclaim responsibility for any injury to people or property resulting from any ideas, methods, instructions or products referred to in the content.